

Meteoric water and glacial melt~~Glacial Meltwater~~ in the Southeast Amundsen Sea: A timeseries from 1994-2020

Andrew N. Hennig¹, David A. ~~Mucciarone~~²Mucciarone⁺, Stanley S. ~~Jacobs~~³Jacobs², Richard A. ~~Mortlock~~⁴Mortlock², Robert B. ~~Dunbar~~²Dunbar⁺

5 ¹Earth System Science, Stanford University, Stanford, California, 94305, USA

²Oceans, Stanford University, Stanford, California, 94305, USA

³Lamont²Lamont-Doherty Earth Observatory, Columbia University, Palisades, New York, 10964, USA

⁴Earth³Earth and Planetary Sciences, Rutgers University, Piscataway, New Jersey, 08854, USA

Correspondence to: Andrew N. Hennig (ahennig@stanford.edu)

10 **Abstract.** Ice sheet mass loss from Antarctica is greatest in the Amundsen Sea sector, where ‘warm’
modified Circumpolar Deep Water moves onto the continental shelf and deep seawater melts and thins
the bases of ice shelves hundreds of meters below the sea surface. We use nearly 1000 paired salinity
and oxygen isotope analyses of seawater samples collected on seven expeditions from 1994 to 2020 to
produce a time series of glacial meltwater inventory ~~for~~^{on} the Southeast Amundsen Sea continental
15 shelf. Water column salinity- $\delta^{18}\text{O}$ relationships yield freshwater endmember $\delta^{18}\text{O}$ values from -
 31.3 ± 0.6 – 30.2 ‰ to -28.4 ± 0.8 ‰, consistent with the isotopic composition of local glacial ice. Meteoric
water inventories, consisting of an estimated >92% glacial meltwater by mass, account for 7.6 ± 0.5 m to
 9.2 ± 0.6 m of‰, demonstrating that regional freshwater content is dominated by deep glacial melt. The
meltwater fractions display temporal variability in the basal melting, with 800 m water column, and
20 exhibit greater meltwater inventories from 7.7 m to 9.2 m. This result corroborates recent studies
suggesting interannual variability than trend over the study period, based on the available data. in basal
melt rates of West Antarctic ice shelves and is consistent with the Amundsen region’s influence on
ocean salinity and density downstream in the Ross Sea.

1 Introduction

25 Four decades of observations ~~show~~^{have shown} significant and increasing glacial ice mass loss from
Antarctica (Rignot et al., 2011; Velicogna et al., 2014; Rignot et al., 2019a).~~(Rignot et al., 2011;~~
~~Velicogna et al., 2014; Rignot et al., 2019).~~ A Special Report on the Ocean and Cryosphere in a
Changing Climate (SROCC) projected 0.61 m to 1.10 m of sea level rise (SLR) by 2100 under RCP8.5
30 forcing, with uncertainty largely hinging on the future of the Antarctic ice sheet (IPCC, 2022). Over the
past two decades, losses from the West Antarctic Ice Sheet (WAIS) ~~have~~ comprised $84 \pm 12\%$ of the total
Antarctic contribution to SLR (5.5 ± 2.2 mm from 1993-2018~~em, since 1901~~; WCRP Global Sea Level
Budget Group, 2018), with glaciers flowing into the Amundsen Sea Sector (particularly the Pine Island
and Thwaites glaciers) dominating the overall negative mass balance of the ice sheet (Rignot et al.,
2019b; Shepherd et al., 2019).

35

~~dominating the overall negative mass balance of the ice sheet (Shepherd et al., 2019). High ice shelf basal melt rates in the Southeast (SE) Amundsen Sea have been linked to the flow of ‘warm’ and salty modified Circumpolar Deep Water (mCDW) onto the continental shelf, separated by cooler but fresher waters above by a thermocline between 300 m and 700 m (Dutrieux et al., 2014; Jacobs et al., 2011). mCDW flows from the continental shelf break towards SE Amundsen Sea ice shelves via “central” and “eastern” glacially-carved bathymetric troughs (Nakayama et al., 2013). This ‘warm’ mCDW penetrates and its penetration into sub-ice shelf cavities (Jacobs et al., 1996; Paolo et al., 2015; Pritchard et al., 2012)(Jacobs et al., 1996; Paolo et al., 2015; Pritchard et al., 2012) where it can access ice shelf grounding lines (Rignot and Jacobs, 2002). To access the Pine Island Ice Shelf (PIIS) grounding line, mCDW passes between the bottom of the ice shelf at ~350 m and a seafloor ridge at ~700 m (Jenkins et al., 2010). Basal melt is driven by total heat transport, dependent more on the thickness of the mCDW layer transported on-shore than its temperature (Dutrieux et al., 2014; Jenkins et al., 2018), with the thickness controlled by local wind forcing of a shelf break undercurrent, in turn influenced by the Amundsen Sea Low. Despite the strong sensitivity of these ice shelves to ocean forcing, and evidence of increasing mass loss in this region, however estimates of Antarctic SLR contributions from basal melt remain poorly constrained (van der Linden et al., 2021, 2023)(van der Linden et al., 2021, 2023).~~

40

45

50

55

~~While there is evidence for accelerating ice mass loss throughout West Antarctica (e.g. Shepherd et al., 2019) driven largely by ice shelf basal melt (Paolo et al., 2015; Pritchard et al., 2012), some studies have shown greater interannual variability in basal melt rates than increase (Paolo et al., 2018; Holland et al., 2019; Adusumilli et al., 2020; Flexas et al., 2022), and some have even suggested a slowing of basal melt rates (Paolo et al., 2022) and grounding line retreat (Christie et al., 2023). Here we use a method independent of satellite-based measurements to assess the glacial meltwater (GMW) inventory in the coastal water columns of the SE Amundsen Sea.~~

60

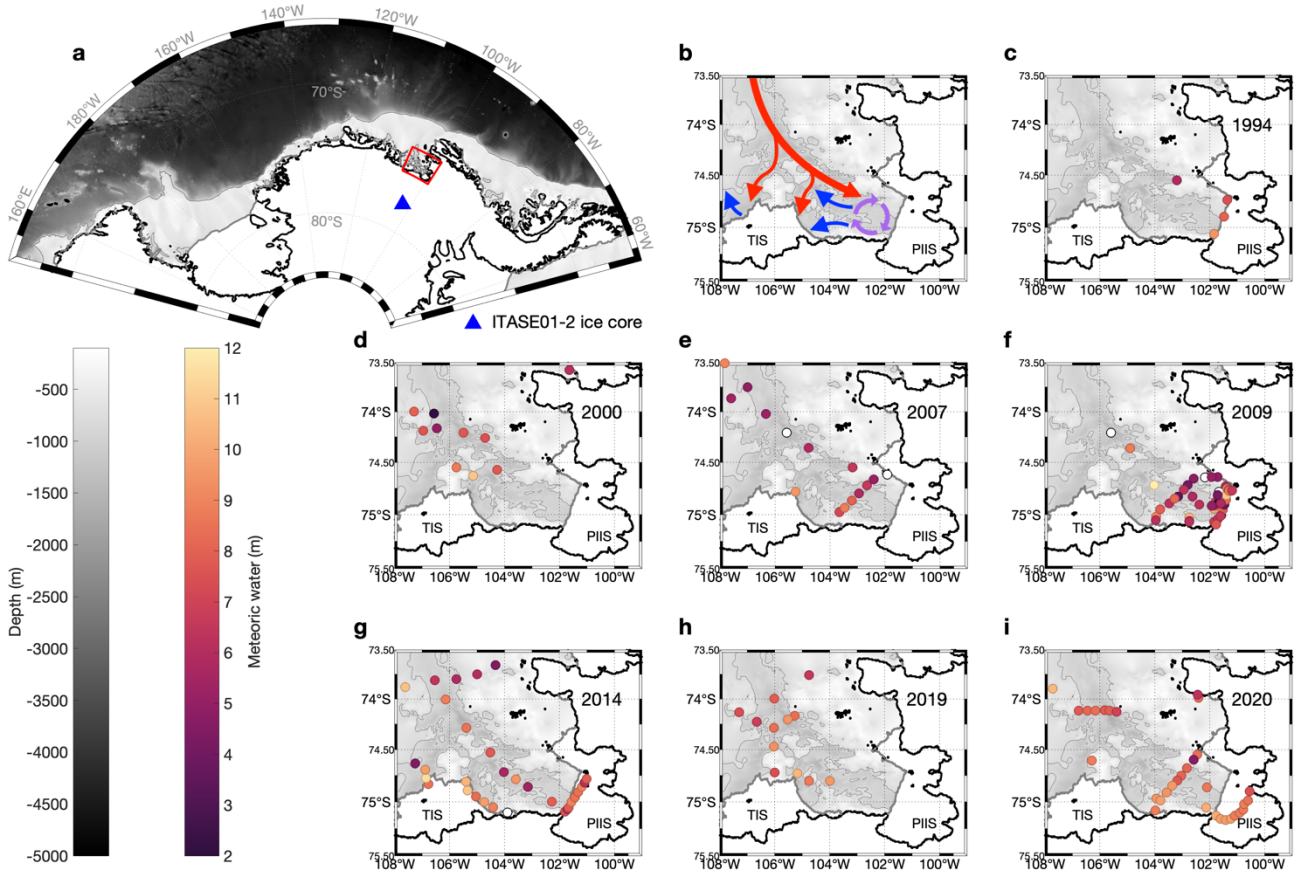
65

70

75

Southern Ocean water masses have typically have been differentiated and defined by measurements of temperature and, salinity, and less often by including oxygen isotopes ($\delta^{18}\text{O}$; Jacobs et al., 1985, 2002; Meredith et al., 2008, 2010, 2013; Brown et al., 2014; Randall-Goodwin et al., 2015; Silvano et al., 2018; Biddle et al., 2019).(~~Jacobs et al., 1985~~). Salinity- $\delta^{18}\text{O}$ relationships can be used to infer the source region and concentration influence of highly $\delta^{18}\text{O}$ -depleted glacial meltwater on seawater properties (Jacobs et al., 1985; Hellmer et al., 1998; Jacobs et al., 2002; Meredith et al., 2008; Randall-Goodwin et al., 2015).~~zero salinity glacial freshwater on seawater properties. Where ice shelf basal melting is deep, meltwater oxygen isotope depletion far exceeds that of local ocean surface precipitation.~~ A spatial and temporal array of T, S and $\delta^{18}\text{O}$ samples can thus be utilized to track GMW content quantity and distribution, especially in nearshore waters adjacent to coastal regions where ice shelf melting ice shelves is strong. Prior studies have used $\delta^{18}\text{O}$ measurements to estimate meteoric water abundance (precipitation and GMW)waters in the Amundsen Sea water column (Biddle et al., 2019; Jeon et al., 2021; Randall-Goodwin et al., 2015) and elsewhere around Antarctica (Meredith et al., 2010, 2018; Silvano et al., 2018) but so far have revealed little about temporal variability or possible trends in GMW glacial meltwater content. Here, we use nearly 1000 seawater isotope samples collected during seven austral summers from 1994 to 2020 (Figure 1~~Figure 1~~) to investigate meteoric

watermeltwater sources, water column inventories, and their interannual variability in the SE Amundsen Sea.



80 **Figure 1: Study area bathymetry, circulation, and $\delta^{18}\text{O}$ sampling locations each of 7 years between 1994 and 2020.**
 85 800 m isobaths are shown as thin gray lines. (a) SE Amundsen study area, and location of the ITASE01-2 ice core. (b) Location of the Pine Island Bay gyre (purple), pathways of warm deep mCDW (red) toward the ice shelves and pathways of shallower meltwater rich waters (blue) from beneath Pine Island Ice Shelf (PIIS; Nakayama et al., 2019; Wählín et al., 2021). (c-i) Colored dots show sample locations, with colors representing vertically integrated glacial meltwater inventories between 0 m and 800 m from 1994 to 2020. Thick gray lines indicate seaward boundaries of Thwaites Ice Shelf (TIS) and the PIIS. Calving fronts are referenced to 2000 (Schaffer et al., 2014; Fretwell et al., 2013), a relatively stable location before a ~20 km retreat following calving events between 2017 and 2020 (Joughin et al., 2021). Stations where sampling did not extend to the seafloor show only partial water column inventories, and stations shown as white dots (2007, 2009, 2014) had only one depth sampled. In 2000, 2007, and 2019, access to sampling along the front of PIIS calving front was precluded by fast ice. - $\delta^{18}\text{O}$ sampling locations each year. (a) SE Amundsen study area, and location of the ITASE01-2 ice core. (b) detailed bathymetry of study location (shading), with isobaths at 500 m and 1000 m (lines). (c-i) Colored dots show sample locations, with colors representing vertically integrated glacial meltwater inventories between 0 m and 800 m from 1994 to 2020. Gray lines indicate seaward boundaries of Thwaites Glacier Tongue (TGT) and the Pine Island Ice Shelf (PIIS). Often limited by fast ice, station locations tend to show higher GMW inventories along or near those calving fronts. The former is referenced to 2000 (Schaffer et al., 2014; Fretwell et al., 2013), a relatively stable location before a ~20 km retreat following calving events between 2017 and 2020 (Joughin et al., 2021a). Stations where depth sampling did not extend to the seafloor show only partial water column inventories.

2 Data and Methods methods

12.1 Sample collection and analysis

100 ~~We compile data from samples~~ Samples were collected during 7 field seasons ~~from sites~~ in the SE
 Amundsen Sea from 1994 to 2020 (~~Figure 1~~~~Figure 1~~, ~~Table 1~~~~Table 1~~). Salinity profiles were obtained
 using calibrated conductivity cells on SBE911 conductivity-temperature-depth (CTD)
 105 ~~instruments~~CTDs, monitored with shipboard bottle sample analyses using Guildline AutoSal and
 PortaSal salinometers calibrated with IAPSO seawater salinity standards. ~~In~~ ~~For most years~~ (1994,
 2007, 2009 and, 2014~~;~~), $\delta^{18}\text{O}$ was measured using an Isotope Ratio Mass Spectrometer (IRMS;
 Micromass Optima Multiprep or a Finnigan MAT252 HDO). All samples collected in 2019 and 2020,
 and some in 2007 and 2009, were measured with a Picarro L2140-i Cavity Ring Down System (CRDS).
 Equivalence has been demonstrated between CRDS and IRMS measurements (Walker et al., 2016;
 110 ~~Appendix A8~~~~A7~~). In all cases, values are reported as per milimille (‰) deviations(δ), relative to
 Vienna Standard Mean Ocean Water (VSMOW2; Coplen, 1994).

Table 1: Summary of $\delta^{18}\text{O}$ data sources, sampling intervals, methods & applications

Year	Cruise	Sample collection dates	# Samples	$\delta^{18}\text{O}$ Technique(s)
1994	NBP94-02	14 Mar. 1994 – 15 Mar. 1994	26	IRMS CO₂ equilibration
<u>1994</u>	<u>NBP94-02</u> (Hellmer et al., 1998)	<u>14 Mar. 1994 – 15 Mar. 1994</u>	<u>26</u>	<u>IRMS CO₂ equilibration</u>
2000	NBP00-01	16 Mar. 2000 – 20 Mar. 2000	62	IRMS CO₂ equilibration
<u>2000</u>	<u>NBP00-01</u> (Jacobs et al., 2002)	<u>16 Mar. 2000 – 20 Mar. 2000</u>	<u>62</u>	<u>IRMS CO₂ equilibration</u>
2007	NBP07-02	24 Feb. 2007 – -27 Feb. 2007	74	IRMS CO ₂ equilibration, CRDS
2009	NBP09-01	16 Jan. 2009 – -29 Jan. 2009	175	IRMS CO ₂ equilibration, CRDS
2014	iSTAR2014	5 Feb. 2014 – 20 Feb. 2014	213	IRMS CO₂ equilibration
<u>2014</u>	<u>iSTAR2014</u> (Biddle et al., 2019)	<u>5 Feb. 2014 – 20 Feb. 2014</u>	<u>213</u>	<u>IRMS CO₂ equilibration</u>
2019	NBP19-01	12 Jan 2019 – 14 Jan 2019	107	CRDS
2020	NBP20-02	5 Feb. 2020 – 8 Mar. 2020	280	CRDS

115 Some of the 2009 samples were processed at Rutgers University in 2010 using a Micromass IRMS; the
 remainder in 2020 using a Picarro CRDS system at Stanford University. While the latter samples had
 not been opened since collection, a substantial number were compromised by evaporation during 11+0
 years of storage. The 2009 samples analyzed in 2020 were scrutinized visually and newly measured
 sample densities compared with those derived from the CTD measurements. Data from compromised

120 samples were discarded (**Appendix A7**). A subset of 100 samples from 2019 and 2020 were processed concurrently using CO₂ equilibration on a Finnigan MAT252 IRMS and CRDS via vaporizer to ensure data comparability between instrumentation (**Appendix A8**). **Measurements A7**. IRMS (CRDS) **measurements** for all years achieved a precision of 0.04‰ for IRMS and (0.02‰ for CRDS,‰) based on replicate analyses.

125 After a review of the literature, we considered a possible salt effect in measured seawater $\delta^{18}\text{O}$, as suggested by a small number of studies Previous studies (Lécuyer et al., 2009; Skrzypek and Ford, 2014; Benetti et al., 2017). As no salt effect offset was applied to the previously published data in this study (1994, 2000, 2014) we have not applied any offset to data from other years. The mCDW $\delta^{18}\text{O}$ value (Table 2) for 2014 is significantly higher than other years (Appendix A2) – likely due to a calibration offset but may also point to sample storage issues. The mCDW and meteoric water endmembers are defined from observations each year, minimizing the impact of interlaboratory offsets on the results (Appendix A2, Data and Methods 2.2). ~~we have observed a possible salt effect offset in measured seawater $\delta^{18}\text{O}$ using both CRDS and IRMS equilibration methods. Benetti et al. (2017) note this salt effect offset is likely to vary between laboratories and analytical methods. As no salt correction was applied to the originally published (1994, 2000, and 2014) data, we have not applied an offset to samples from 2007, 2009, 2019, and 2020. Here, we compare calculated GMW fractions (Data & Methods), rather than direct isotope measurements, minimizing any potential issues arising from offsets between laboratories (Appendix A2).~~

1.2 Meteoric waters defined by the $\delta^{18}\text{O}$ —salinity relationship

140 The zero salinity $\delta^{18}\text{O}$ endmember, defined by data below 200 m, reflects pure meteoric freshwater in the form of ice shelf basal melt (Data and Methods). Freshwater endmembers (intercepts) revealed by salinity- $\delta^{18}\text{O}$ relationships over the seven sampled summers differ by <2‰, ranging from -28.4‰ to -30.2‰ (**Figure 2, Table 2**). These measurements are consistent with the nearest ice core (ITASE01-2, from 77.84°S, 102.91°W, **Figure 1a**; Schneider et al., 2006; Steig et al., 2005) ~~with a mass averaged $\delta^{18}\text{O}$ value of -29.8 ± 1.9 ‰. Ice cores further east have less negative $\delta^{18}\text{O}$ values (-20 ‰; Thomas et al., 2009), while those further west are more negative (-40 ‰; Blunier & Brook, 2001). Local precipitation, in the form of snow collected in early 2019 at 72°S, yielded a $\delta^{18}\text{O}$ value of -15 ‰, consistent with previous observations at sea level from this latitude (Masson-Delmotte et al., 2008). The zero salinity endmembers extrapolated from the regional salinity and $\delta^{18}\text{O}$ observations indicate that freshwater added to the water column is dominated by locally derived GMW, as intimated earlier for the 1994 data (Hellmer et al., 1998).~~

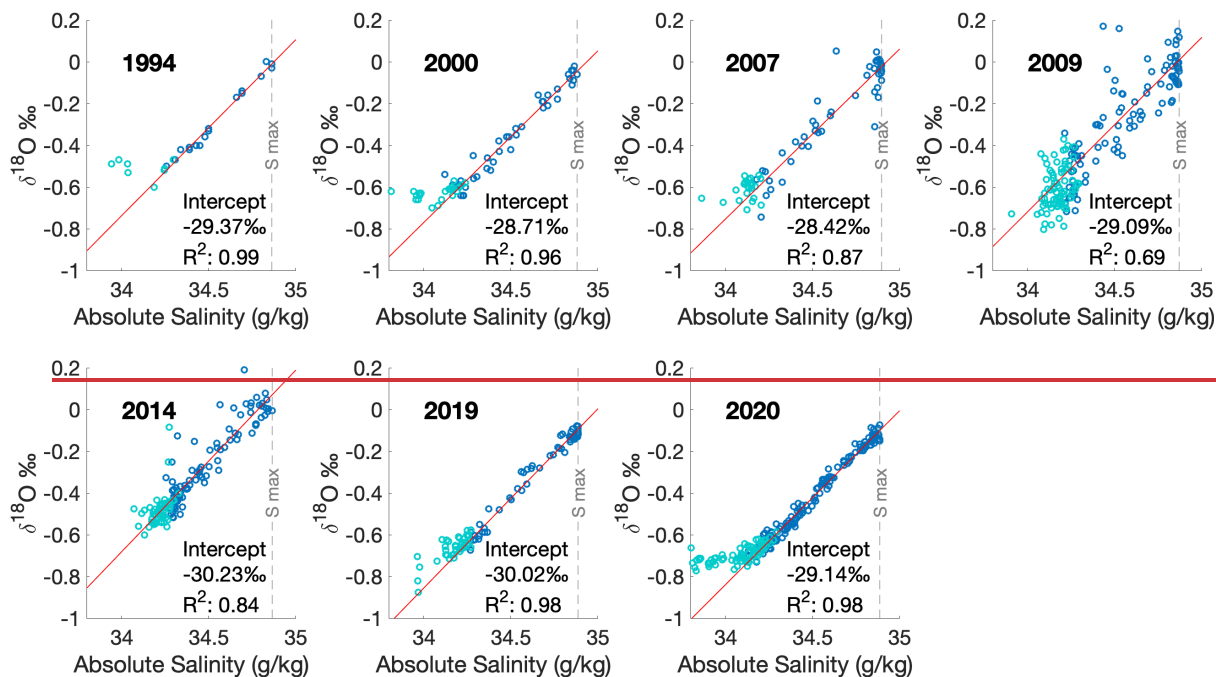


Figure 2: Salinity vs $\delta^{18}\text{O}$ plots for each year. Dark blue circles represent samples deeper than 200 m, fit by linear regression shown as red lines (with R^2 from 0.69 in 2009 to 0.99 in 1994) that project zero salinity glacial meltwater endmember intercepts. Light gray dashed vertical lines indicate the modified Circumpolar Deep Water (mCDW) salinity maxima (Table 2). The most negative upper water column seawater $\delta^{18}\text{O}$ measurements tend to reach minima between -0.8‰ and -0.5‰ . The larger scatter in 2009 and 2014 results likely from sample storage issues (Appendix A6).

1.32.2 Three-endmember mixing model

We adapt an approach from Östlund & Hut (1984) ~~as that has been applied by others~~ in the Peninsula-Bellingshausen-Amundsen region of West Antarctica (Biddle et al., 2019; Jeon et al., 2021; Randall-Goodwin et al., 2015; Meredith et al., 2010) and near ~~the~~ Totten ~~Ice Shelf ice shelf~~ (Silvano et al., 2018). ~~We use a 3-endmember~~ ~~Our~~ mixing model (Equations 1-3) to determine water source fractions in the field area. The model assumes ~~the that~~ observed $\delta^{18}\text{O}$ and salinity values ~~are the result from of~~ mixtures of mCDW, sea ice ~~melting/freezing melt~~, and meteoric waters contributing a range of $\delta^{18}\text{O}$ and salinity signatures. Meteoric waters ~~deeper than 200 m deep below the surface~~ are dominated by ice shelf basal melt, ~~as are surface waters near the ice shelves~~. ~~Shallower but moving toward shallower~~ depths in the water column, ~~can will~~ also include ~~ice front/wall melt~~, and iceberg melting. ~~Near; near-~~near-surface waters ~~are also influenced by sea ice melt and formation, and are likely to will~~ contain ~~both some amount of~~ local ~~and advected sea level~~ precipitation.

Equations 1-3: Three-endmember mixing model. The 3-endmember mixing model uses the absolute salinity and $\delta^{18}\text{O}$ of mCDW, sea ice melt, and meteoric water endpoints to solve for the relative ~~fractions abundance~~ of the three water ~~sources masses~~ in each sample analyzed.

$$f_{sim} + f_{met} + f_{mcdw} = 1 \quad (1)$$

$$f_{sim} * S_{sim} + f_{met} * S_{met} + f_{mcdw} * S_{mcdw} = S_{obs} \quad (2)$$

$$f_{sim} * \delta_{sim} + f_{met} * \delta_{met} + f_{mcdw} * \delta_{mcdw} = \delta_{obs} \quad (3)$$

175
 180
 185
 190
 195
 200
 205
 210

f = fraction of water source
 S = salinity
 δ = $\delta^{18}\text{O}$
 sim = sea ice melt
 met = meteoric water
 $mcdw$ = modified circumpolar deep water
 obs = observed sample

The primary fraction of interest is the meteoric water fraction comprised of ice shelf melt. The meteoric water endmember is defined as the zero-salinity $\delta^{18}\text{O}$ intercept of data below 200 m (). This intercept reflects the average $\delta^{18}\text{O}$ of pure meteoric freshwater in the form of ice shelf basal melt (Results 3.1, Appendix A1). Below 200 m the $\delta^{18}\text{O}$ -salinity plots yield mixing lines with mCDW as the saltiest, least-depleted component, and meteoric water as the most highly depleted freshwater endmember, indicative of basal meltwater. To minimize issues that could arise from inter-laboratory calibration offsets (Data and Methods 2.1, Appendix A2), we define individual mCDW and meteoric water endmembers separately for each year (Table 2). Model outputs (mCDW, meteoric water, and sea ice melt fractions) critically depend on appropriate endmember inputs, which will affect resulting water source fractions and trends.~~The primary fraction of interest is that of ice shelf basal and wall meltwater fractions, defined at the zero-salinity intercepts on $\delta^{18}\text{O}$ -salinity plots of all samples taken each year (Figure 2). Below the surface mixed layer, more generally influenced by sea ice melt and local precipitation, the $\delta^{18}\text{O}$ -salinity plots yield mixing lines with mCDW as the saltiest, least-depleted component, and glacially-derived meteoric water as a highly depleted freshwater endmember. The zero-salinity intercepts extrapolated from these lines represent the mean $\delta^{18}\text{O}$ properties of basal ice being melted by warm mCDW. This approach differs somewhat from other studies (Biddle et al., 2019; Meredith et al., 2010) that estimate meteoric water content from approximate glacier $\delta^{18}\text{O}$ values.~~

The mCDW is the warmest, saltiest, and least $\delta^{18}\text{O}$ -depleted water mass in the region and comprises the vast majority of the overall water column. Interannual changes in mCDW inflow will result from variable wind forcing (Dotto et al., 2019; Holland et al., 2019; Kim et al., 2021), combined with on-shelf lateral and vertical mixing. While mCDW incorporates a range of salinities, temperatures, and $\delta^{18}\text{O}$ values, in the Amundsen Sea it is the warmest, saltiest, and deepest water mass. In the 3-endmember mixing model, mCDW and meteoric waters are defined by the mixing line of data >200m; with mCDW separately for each year (Table 2) based on the $\delta^{18}\text{O}$ value values at the salinity maximum (Biddle et al., 2017) and meteoric water the 0-salinity zero-salinity intercept on the mixing line (Results 3.1;).~~mCDW-glacial meltwater mixing line (Figure 2). Sea ice endmember isotopic values adopted from previous studies in the Amundsen and Bellingshausen region (Meredith et al., 2008, 2010, 2013; Randall-Goodwin et al., 2015; Biddle et al., 2019)(Randall-Goodwin et al., 2015; Meredith et al., 2008)~~

215 are based on the $\delta^{18}\text{O}$ of surface water with an offset to account for isotopic fractionation (-2.1‰) due to freezing.

220 **Table 2:** Salinity and $\delta^{18}\text{O}$ values used in the 3-endmember mixing model. mCDW and meteoric components are defined independently using the mCDW-GMW mixing line produced from ($>200\text{ m depth}$) salinity and $\delta^{18}\text{O}$ observations for each year, as the salinity maximum and 0-salinity-zero-salinity intercept, respectively (Results 3.1; (Figure 2; Appendix A1).A1). Sea ice melt uses single values for each year. Salinities are reported as absolute salinity (g/kg).

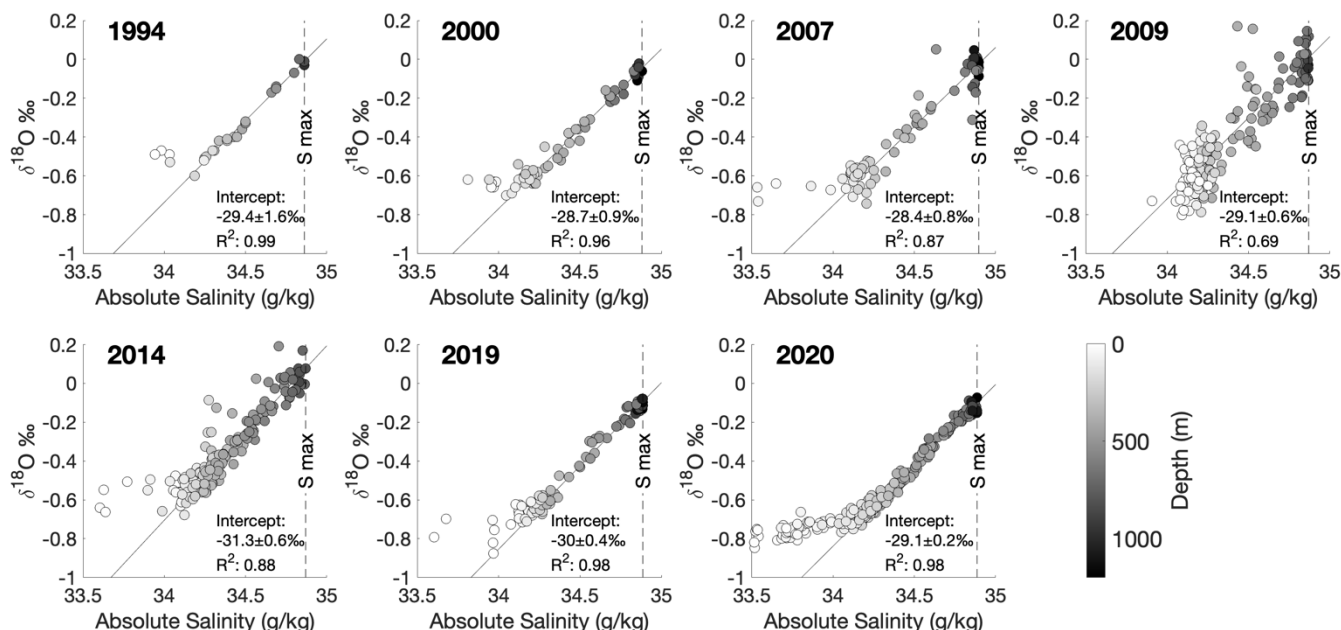
Year	mCDW salinity (g/kg)	mCDW $\delta^{18}\text{O}$ (‰)	Meteoric water (GMW) $\delta^{18}\text{O}$ (‰)	Sea ice melt salinity (g/kg)	Sea ice melt $\delta^{18}\text{O}$ (‰)
1994	34.86 \pm 0.010	-0.01 \pm 0.01	-29.4 \pm 1.4		
2000	34.86 \pm 0.011	-0.05 \pm 0.01	-28.7 \pm 0.6		
2007	34.89 \pm 0.009	-0.02 \pm 0.02	-28.4 \pm 0.8		
2009	34.87 \pm 0.002	0.01 \pm 0.02	-29.1 \pm 0.6	7	2.1
2014	34.85 \pm 0.015	0.08 \pm 0.01	-31.3 \pm 0.5		
2019	34.88 \pm 0.006	-0.09 \pm 0.01	-30.0 \pm 0.4		
2020	34.87 \pm 0.017	-0.10 \pm 0.01	-29.1 \pm 0.2		

3 Results

3.1 Meteoric waters defined by the $\delta^{18}\text{O}$ – salinity relationship

225 Freshwater endmembers (zero-salinity $\delta^{18}\text{O}$ intercepts) over the seven sampled summers differ by $<3\text{‰}$, ranging from -28.4‰ to -31.3‰ with a standard deviation of 1.0‰ (, Table 2). These measurements are consistent with the nearest ice-core (ITASE01-2, from 77.84°S , 102.91°W , Figure 1a; Schneider et al., 2006; Steig et al., 2005) Deep introduction of GMW is consistent with subglacial melt) with a mass-averaged $\delta^{18}\text{O}$ value of $-29.8\pm 1.9\text{‰}$. Ice cores further east have less negative $\delta^{18}\text{O}$ values ($\sim 20\text{‰}$; Thomas et al., 2009), while those further west are more negative ($\sim 40\text{‰}$; Blunier & Brook, 2001). Intercept uncertainty from analytical precision and environmental variability (Appendix A3) ranges from $\pm 0.2\text{‰}$ in 2020 to $\pm 1.4\text{‰}$ in 1994, varying inversely with the number of data points available.

235 Local precipitation, in the form of snow collected in early 2019 at 72.5°S , yielded a $\delta^{18}\text{O}$ value of $\sim 15\text{‰}$, consistent with previous observations and model outputs at sea-level from that latitude (Masson-Delmotte et al., 2008). Endmember extrapolations from the regional salinity and $\delta^{18}\text{O}$ measurements indicate that freshwater added to the water column is dominated by locally derived GMW, as intimated earlier from 1994 data (Hellmer et al., 1998).



240 **Figure 2: Salinity vs $\delta^{18}\text{O}$ plots for each year, shaded by depth.** Linear regressions (solid) gray lines (with R^2 from 0.69 in 2009 to 0.99
 245 in 1994) project to zero-salinity glacial meltwater endmember intercepts using data $>200\text{m}$. Dashed vertical lines indicate the mCDW
 salinity maxima (Table 2). Data diverge from the mCDW-meteoric water mixing line in the upper water column, where sea ice melt
 freshens the resultant mixture but has an enriching effect on $\delta^{18}\text{O}$ (Table 2). Years with greater divergence at the surface have more sea ice
 melt (Appendix A6). The most negative upper water column seawater $\delta^{18}\text{O}$ measurements tend to reach minima between -0.9‰ and
 250 -0.6‰ .

255 Samples below 200 m show a strong $\delta^{18}\text{O}$ -salinity relationship, forming a mixing line between mCDW and a (glacial) meteoric freshwater endmember introduced at depth. Closer to the surface (from 10 m in 2009 to 160 m in 2000) data diverge from the mixing line due to the net influence of sea ice melt and local precipitation, moving the $\delta^{18}\text{O}$ of the mixture in a more positive direction. Below 200m the $\delta^{18}\text{O}$ -salinity relationship is strongly linear; greater scatter in 2009 and 2014 likely results from sample storage issues (Appendix A7).

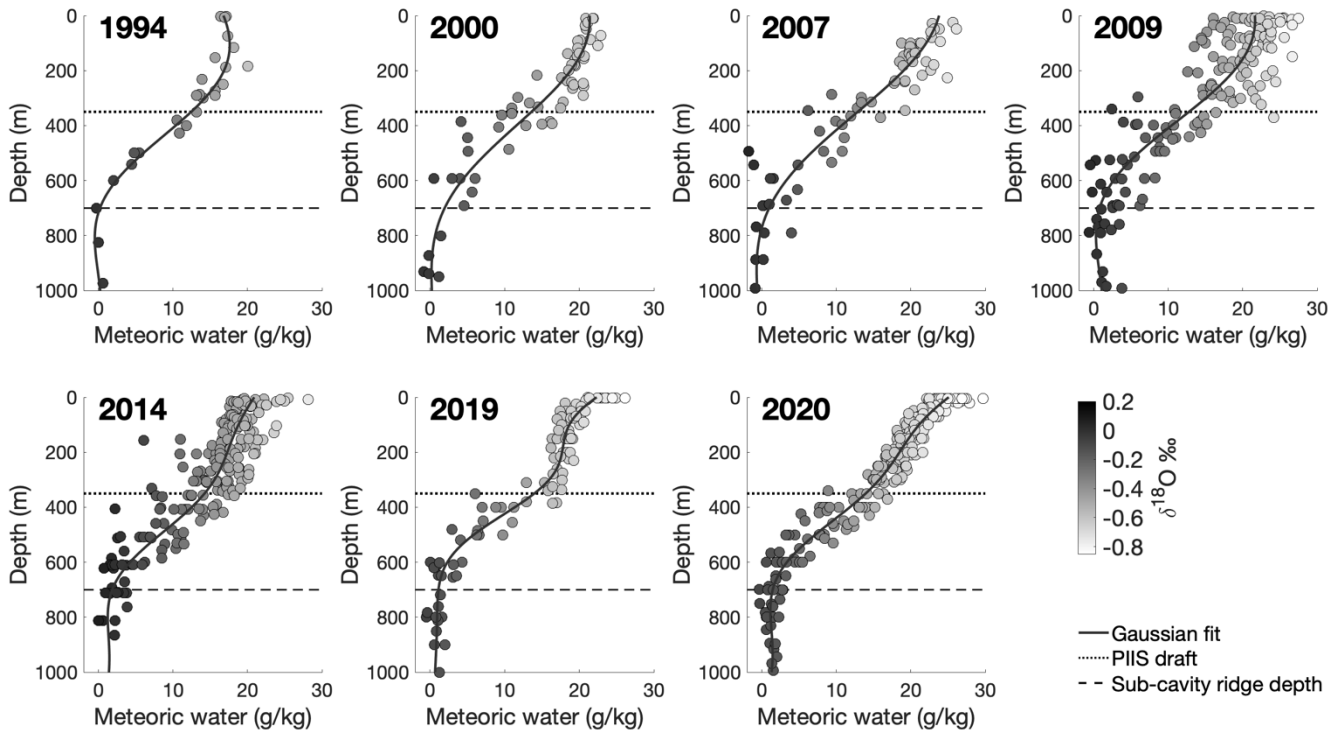
255 In 2009 and 2014, samples were collected in bottles with taped (2009) or parafilm-wrapped (2014), threaded caps, and stored for several years before analysis. Samples from 2019 and 2020 were collected in glass serum vials capped with rubber stoppers and aluminum seals (Appendix A9), which internal lab data demonstrate the maintenance of seawater $\delta^{18}\text{O}$ sample integrity for 5+ years. Scatter occurs mostly in the positive $\delta^{18}\text{O}$ direction (particularly in 2014), indicative of sample evaporation.

4.43.2 Vertical distribution of meteoric water illustrates basal melt

260 A 3-endmember mixing model of mCDW, sea ice melt, and meteoric water ~~is can be~~ used to determine the constituent freshwater components of seawater (Equations 1 Equations 1-3) at all depths sampled in the water column (Figure 3 Figure 3). ~~By using We compare the derived GMW fractions that are~~

265

calculated from separately defined mCDW and meteoric water GMW values for each year. Using mCDW and GMW endmember values based on annual data from each year individually, minimizing the potential impact of mean the calculated GMW fractions are extremely unlikely to be impacted by analytical calibration offsets between laboratories on the calculated meteoric water fractions. (Data and Methods 2.1; Appendix A2).A2).



270

Figure 3: Meteoric water fractions (g/kg) vs depth. Shading shows $\delta^{18}\text{O}$ value, and solid lines represent Gaussian Process regression fits. Dotted and dashed lines show the depth of the PIIS draft and sub-cavity ridge (Jenkins et al., 2010). Slightly negative meteoric water values at depth occur when the sample exceeds the mCDW endmember value (Table 2; Data and Methods 2.2), the result of environmental, sampling and analytical uncertainties (discussed in further detail in Results 3.4). **Glacial meltwater fractions (g/kg) in the SE Amundsen Sea water columns.** Red lines represent Gaussian Process regression fits. Small negative GMW values at depth in some years are mathematical artifacts that occur when the sample $\delta^{18}\text{O}$ is higher than that of the mCDW endmember (Table 2, Data and Methods).

275

280

Evidence of highly $\delta^{18}\text{O}$ -depleted freshwater is found at depths above ~ 700 m (the depth of PIIS sub-ice shelf ridge; Jenkins et al., 2010), with highest concentrations found at depths shallower than 350 m – above which glacial meltwater has been observed to flow out from beneath the ice shelf (Biddle et al., 2017; Naveira Garabato et al., 2017). Made less dense by the addition of GMW, such outflows rise through denser waters above, along ice shelf calving fronts and strongly influencing surface waters in this region. Evidence of highly $\delta^{18}\text{O}$ -depleted freshwater is found at depths shallower than 800 m, increasing rapidly upward from ~ 600 m to the surface or its mixed layers (Figure 3). The mean depth of the Pine Island Ice Shelf calving front was about 400 m in 2009 (Jenkins et al., 2010). Outflows from such depths, lightened by the addition of GMW, rise through denser waters above, along ice shelf

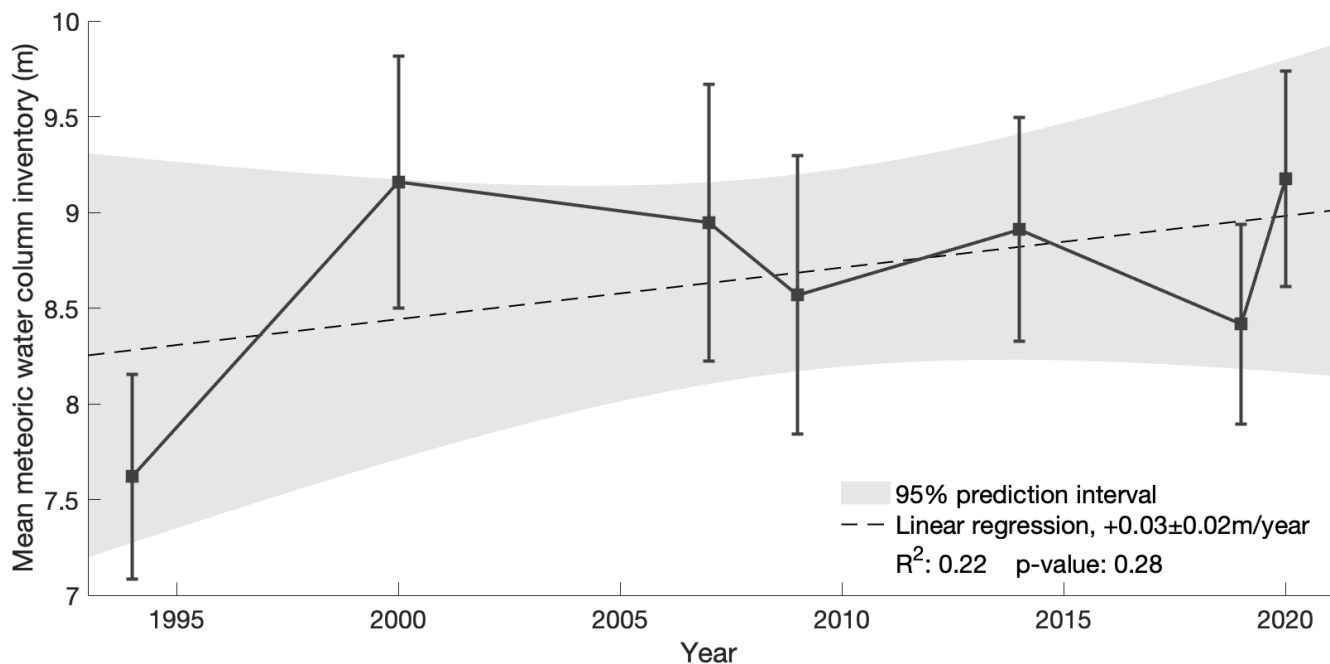
285 ~~calving fronts (Dierssen et al., 2002; Mankoff et al., 2012; Thurnherr et al., 2014; Fogwill et al., 2015). Depending on the extent of mCDW heat remaining after basal melting, that will contribute to the formation of coastal polynyas (Mankoff et al., 2012) and surface layer $\delta^{18}\text{O}$ minima. Where GMW ends up in coastal water columns depends on its production rate, impact on the density of circulating water, and access of return flows to the ice shelf calving fronts.~~

290 ~~Sea ice melt and mCDW fractions are discussed in [Appendix A6](#).~~

1.53.3 Average meteoric water GMW inventory over the last two decades

295 ~~Average meteoric water column inventories ([Table 3](#)) in the study area were estimated by depth integrating the Gaussian Process fit of the calculated meteoric water fractions (solid lines in [Figure 3](#)). The average meteoric water column inventory was relatively low in 1994 and higher from 2000-2020. Strongly influenced by the low meteoric water inventory in 1994, a linear regression of the mean meteoric water inventories suggests an increase of 0.03 ± 0.02 m/y (p-value 0.28). Meteoric water column inventories have uncertainties of <0.8 m, based on analytical precision and environmental~~
300 ~~variability of the model inputs ([Results 3.4](#)). Assuming 1 m water equivalent (2 years) of precipitation (Boisvert et al., 2020; Donat-Magnin et al., 2021), the meteoric water inventories are likely to consist of $>92\%$ GMW ([Appendix Error! Reference source not found.](#)).~~

305 ~~Regional average GMW column inventories were estimated by depth integrating the Gaussian Process fit of the calculated meteoric water fractions (red lines in [Figure 3](#)). The average GMW inventory was relatively low in 1994 and high in 2000 and 2020, with an uncertainty of ≤ 0.7 m in an overall average of 8.60 m; $\sim 1\%$ the upper 800 m water columns. Though largely a product of the low GMW inventory in 1994, a linear regression of the mean GMW inventories produces a modest increase of 0.02 m/y. Observations indicate the mCDW responsible for basal melt does not exhibit significant seasonal~~
310 ~~variability in this region (Mallett et al., 2018), and A related study showed mostly invariable overall melt rates during austral summer (Kimura et al., 2017), when the samples used in this study were collected ([Table 1](#)).~~



315 **Figure 44: Average meteoric water GMW column inventory in study area.** Depth-integrated meteoric water content GMW volume from the Gaussian Process fit (see Figure 3) between the sea surface and 800 m depth. Error bars show the uncertainty (Table 3) in mean GMW column inventory associated with data volume, analytical precision, and uncertainty in endmember values (Data and Methods 2.2). A linear regression of the mean values shows an average increase of 0.03 ± 0.02 m/year (p-value 0.28). Grey shading shows the 95% prediction interval for the linear regression.

320

1.63.4 Uncertainty and sensitivity analyses

3.4.1 Analytical precision and environmental variability

325

Comparing GMW content and $\delta^{18}\text{O}$ -salinity relationships between different groups of stations, we found that sample location variability had an insignificant impact on calculated average meteoric water content, except for 2014, when the stations along the edge of TGT had considerably higher GMW content. In the interest of improving interannual comparability, 2014 stations closest to TGT were excluded from the average GMW content analyses (Appendix A4).

330

We ran 10,000 Monte Carlo simulations where observations were perturbed around their measured value by on each data point to test for sensitivity to variance in mCDW properties, endmember uncertainty associated with, and analytical precision (0.04‰ $\delta^{18}\text{O}$ for IRMS; 0.02‰ $\delta^{18}\text{O}$ for CRDS; 0.002 g/kg salinity) and water source endpoints (mCDW, sea ice melt, meteoric water). mCDW and meteoric water endpoints were defined using perturbed observational data for each simulation, and around the selected endpoint by in the 3-endmember GMW fraction model. Each observed value and water mass endpoint was varied around the reported value by the analytical and environmental

335

uncertainty associated with that tracer (Appendix A3). Zero-salinity intercept (meteoric endmember) uncertainty associated with environmental variability (Table 3, Appendix A3). analytical precision ranges from $\pm 0.48\%$ in 2020 to $\pm 1.62\%$ in 1994, varying inversely with the number of data points available for the extrapolation. Uncertainty in mean meteoric water GMW fractions ranges from 1.1 was ± 1 g/kg in 2019 to ± 1.7 g/kg in 2007, corresponding to ± 0.5 – 0.7 m (± 6 – 8%) 2009, and uncertainty in mean meteoric column inventories ranges from 6-9%.

water column GMW inventory (Gaussian Process fit, red lines in Figure 3; Appendix A3) with 2009 exhibiting the greatest uncertainty, and 2020 the least. Calculated water GMW fractions are most strongly influenced by changes made to the mCDW endmember (comprising $\sim 99\%$ of an 800m water column on average; $\sim 95\%$ in surface waters rich in meteoric water and sea ice melt). Meteoric water fractions vary inversely with the magnitude of the meteoric water endmember $\delta^{18}\text{O}$. 1994 has the fewest samples, but the strongest fit (r^2), and exhibits similar uncertainty to other years (Figure 4).

Table 3: Meteoric water column inventory analytical and environmental uncertainty. Depth-integrated meteoric water content using the Gaussian Process fit (Figure 3) between the sea surface and 800 m depth. Uncertainties are associated with number of data points, analytical precision, and environmental variability in endmember values (Data and Methods 2.2).

Year	Meteoric water fraction uncertainty (g/kg)	Meteoric water column inventory (m)	% meteoric water column inventory uncertainty
1994	1.5	7.6 \pm 0.5	7.0%
2000	1.7	9.2 \pm 0.7	7.2%
2007	1.7	8.9 \pm 0.7	8.1%
2009	1.7	8.6 \pm 0.7	8.5%
2014	1.5	8.9 \pm 0.6	6.6%
2019	1.1	8.4 \pm 0.5	6.1%
2020	1.2	9.2 \pm 0.6	6.1%

3.4.2 Spatial variability

This study relied on the compilation of data collected for 6 independent studies over 7 different cruises. To determine the impact of inconsistency in sampling locations each year, two different spatial sensitivity analyses were used. First, we conducted 10,000 simulations, for each year selecting random sets of 3 stations within the field area. In each case, mCDW and meteoric water endmembers, and mean meteoric water column inventories were calculated using only those data. Uncertainty is represented as the standard deviation of those results (Table 4).

Table 4: Results of randomized spatial sensitivity analysis. Uncertainty is represented by the standard deviation of the results of 10,000 simulations for each year, calculating results using data from only 3 randomly selected stations.

Year	mCDW absolute salinity (g/kg)	mCDW $\delta^{18}\text{O}$ (‰ vs VSMOW)	mCDW potential temperature (°C)	Meteoric water $\delta^{18}\text{O}$ (‰ vs VSMOW)	Average meteoric water column inventory (m)	Meteoric water fraction uncertainty (g/kg)
------	-------------------------------	---	---------------------------------	---	---	--

1994*	<u>34.86±0</u>	<u>-0.01±0.01</u>	<u>1.08±0.01</u>	<u>-29.4±0.6</u>	<u>7.6±0.2</u>	<u>0.1</u>
2000	<u>34.86±0.012</u>	<u>-0.06±0.02</u>	<u>1.03±0.07</u>	<u>-28.7±1.6</u>	<u>8.8±0.5</u>	<u>0.8</u>
2007	<u>34.89±0.009</u>	<u>-0.03±0.04</u>	<u>1.18±0.03</u>	<u>-27.8±3.4</u>	<u>9.0±0.7</u>	<u>1.1</u>
2009	<u>34.87±0.002</u>	<u>-0.01±0.06</u>	<u>1.17±0.01</u>	<u>-28.9±4.1</u>	<u>8.8±0.7</u>	<u>1.8</u>
2014	<u>34.85±0.015</u>	<u>0.05±0.03</u>	<u>1.10±0.04</u>	<u>-31.2±3.3</u>	<u>8.5±0.8</u>	<u>1.1</u>
2019	<u>34.88±0.006</u>	<u>-0.10±0.01</u>	<u>1.08±0.06</u>	<u>-29.6±1.6</u>	<u>8.5±0.4</u>	<u>0.6</u>
2020	<u>34.87±0.017</u>	<u>-0.12±0.02</u>	<u>1.03±0.01</u>	<u>-29.0±1.4</u>	<u>8.8±0.6</u>	<u>0.7</u>

* As 1994 has only 4 sampling locations, and the strongest fit of any year () its uncertainty may be artificially decreased

Additionally, we conducted a spatial sensitivity analysis by separately analyzing different spatial groups of stations across each year (Figure 5, Table 5), running 10,000 Monte Carlo analyses for each group as described in Results 3.4.1. Uncertainty is represented as the standard deviation of those results (Table 5, Table A2).

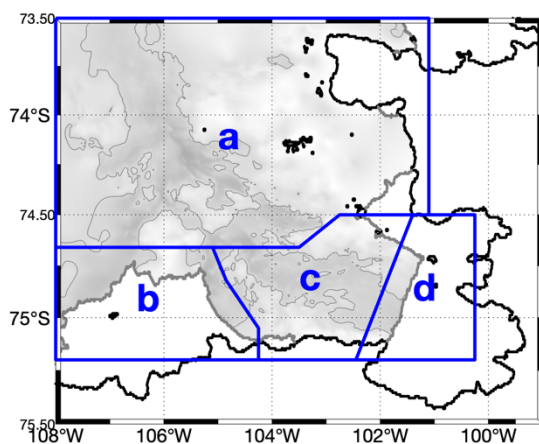


Figure 5: Boundaries of geographic groupings used for spatial sensitivity analysis. Blue lines show boundaries of geographic areas analyzed separately. Gray shading shows bathymetry, with isobaths drawn at 800m. More detailed maps for each year are in Appendix A4.1.

Table 5: Summarized results of meteoric water column inventory (m) from spatial sensitivity analysis (Figure 5). Results by year in rows, and by area group in columns. See Appendix A4.1 for further detail.

	a	b	c	d
1994	<u>6.3±0.5*</u>	-	-	<u>8.0±0.6</u>
2000	<u>9.2±0.7</u>	-	-	-
2007	<u>8.4±0.8</u>	<u>10.3±0.8*</u>	<u>9.0±0.7</u>	-
2009	<u>7.0±0.6*</u>	-	<u>8.7±0.8</u>	<u>8.5±0.7</u>
2014	<u>8.3±0.6</u>	<u>10.1±0.7</u>	<u>7.9±0.5</u>	<u>7.5±0.5</u>
2019	<u>8.2±0.6</u>	<u>10.0±0.7</u>	<u>8.2±0.5</u>	-
2020	<u>8.7±0.6</u>	-	<u>8.7±0.5</u>	<u>8.5±0.5</u>

* Data from only one station. For 1994, 2007, and 2009, result is based on only 8, 4, and 4 samples, respectively.

Both sets of spatial sensitivity analyses show little spatial variability in calculated endmember values or mean meteoric water column inventories, possibly excepting 2009, where there are known sample quality concerns. Mean meteoric water column inventories are remarkably consistent spatially, except

385 those calculated from stations in Group b alongside the TIS, which showed significantly higher
meteoric water inventories than the rest of the study area. Although only 1 and 2 stations alongside the
TIS were sampled in 2007 and 2019, the average column inventories are consistent with the 2014 data,
390 where there were 8 stations in Group b. The higher inventories in Group b are suggestive of an
accumulation of basal melt, and consistent with findings from another study showing that basal melt
from beneath PIIS ends up along the eastern edge of TIS (Wåhlin et al., 2021). The relative insensitivity
of sampling location (except for those alongside TIS) in calculated mean meteoric water column
inventories suggests that precise reoccupation may be unnecessary, and potentially that a relatively
small number of stations/samples could be used to reliably assess mean meteoric water column
inventory in this region.

4 Discussion

4.1 The utility of zero-salinity $\delta^{18}\text{O}$ intercepts

395 The meteoric water endmember has been described as the least well-constrained component (Meredith
et al., 2008, 2010, 2013; Randall-Goodwin et al., 2015; Biddle et al., 2019) of the three-endmember
mixing model employed here, leading previous studies to use plausible mean meteoric $\delta^{18}\text{O}$ values,
falling between the $\delta^{18}\text{O}$ value of glacial melt and local precipitation. However, $\delta^{18}\text{O}$ -salinity plots
presented here () show mixing diagrams of different water sources in the SE Amundsen Sea and suggest
400 that the meteoric endmember for waters below the surface mixed layer can be well-constrained. mCDW
is the saltiest, and least-depleted water, while glacial meltwater is fresh and the most depleted in $\delta^{18}\text{O}$.
Data from deeper than 200 m fall along a mixing line between mCDW and a meteoric freshwater source
with a $\delta^{18}\text{O}$ value indicative of local glacial freshwater (Steig et al., 2005; Schneider et al., 2006), with
lower uncertainty than the mass-weighted standard deviation of the average $\delta^{18}\text{O}$ of the ITASE01-2 ice
core ().

405 The 2014 data here was previously used in another study (Biddle et al., 2019), where they selected -
25‰ as a meteoric water $\delta^{18}\text{O}$ endmember. In comparison to the meteoric endmember used in this study
(-31.3‰ for 2014), a -25‰ endmember results in overestimating mean (800 m water column) meteoric
water content by 2 m (23%), and underestimating mean sea ice melt by 2.9 m – changing the signal
410 from one of net sea ice melt (this study) to one of net formation (Biddle et al., 2019). The -25‰
endmember was selected as a “mean” meteoric water endmember midway between the $\delta^{18}\text{O}$ of GMW
and precipitation as defined in another study (Randall-Goodwin et al., 2015). We estimate that >92% of
the meteoric water in the study area is GMW (Discussion 4.2, Appendix Error! Reference source not
found.). Determining the meteoric water endmember using the better-constrained zero-salinity $\delta^{18}\text{O}$
415 intercept of the sample data mixing line (Data and Methods 2.2) provides more accurate meteoric
water and sea ice melt fractions. The length of the intercept extrapolation emphasizes the importance of
careful sample collection, storage, and high-precision analyses.

4.2 Basal meltwater and precipitation

420 Precipitation grows increasingly depleted in ^{18}O with latitude (Dansgaard, 1964; Gat and Gonfiantini, 1981; Ingraham, 1998; Masson-Delmotte et al., 2008) and altitude (Dansgaard, 1964; Friedman and Smith, 1970; Siegenthaler and Oeschger, 1980; Ingraham, 1998; Araguás-Araguás et al., 2000; Sato and Nakamura, 2005; Masson-Delmotte et al., 2008). Most (88%) of spatial variation in the $\delta^{18}\text{O}$ of Antarctic precipitation can be explained by linear relationships between latitude, elevation, and distance from the coast, with elevation being the primary driver (Masson-Delmotte et al., 2008). Precipitation collected during the NBP19-01 cruise in the study had a $\delta^{18}\text{O}$ value of -15‰ , consistent with other data from that latitude and elevation (Gat and Gonfiantini, 1981; Ingraham, 1998; Noone and Simmonds, 2002; Masson-Delmotte et al., 2008). Precipitation collected at Halley Bay (75.58°S , 20.56°W , 30m elevation) has an average composition of $-22.0\pm 5.6\text{‰}$, while that collected at Rothera Point (67.57°S , 68.13°W , 5m elevation) has an average composition of $-13.5\pm 3.4\text{‰}$, and precipitation collected at Vernadsky (65.08°S , 63.98°W , 20m elevation) has an average composition of $-10.2\pm 3.0\text{‰}$ (Global Network of Isotopes in Precipitation (GNIP), 2023).

435 The nearest Ice cores to our site (ITASE01-2, Steig et al., 2005; Schneider et al., 2006; Siple, Mosley-Thompson et al., 1990) have average $\delta^{18}\text{O}$ compositions of $-29.6\pm 1.6\text{‰}$. Using locally collected salinity and $\delta^{18}\text{O}$ data from deeper than 200 m to calculate a zero-salinity intercept, we identify average freshwater endmembers ranging from $-31.3\pm 0.8\text{‰}$ to $-28.4\pm 0.8\text{‰}$ (average $29.3\pm 0.7\text{‰}$). The similar zero-salinity intercept, and strong linear salinity- $\delta^{18}\text{O}$ relationship below 200 m demonstrates that glacial freshwater is responsible for the observed freshening signal. We find roughly half of the total meltwater inventory in the upper 200 m, below which inventories yield the same general trend in interannual variability (Appendix A5). This indicates the observed variability results from changes in glacial meltwater content, and not from interannual variability in local precipitation.

445 The Pine Island/Thwaites area receives ~ 0.5 m/y (water equivalent) of precipitation (Donat-Magnin et al., 2021), and the residence time of deep shelf waters here is ~ 2 years (Tamsitt et al., 2021). We recalculated our meteoric water column inventories assuming 2 years' worth of local precipitation ($\delta^{18}\text{O}$ -15‰) in the upper 200 m, and find that on average, the addition of precipitation decreases the meteoric water ($\delta^{18}\text{O}$ $\sim -30\text{‰}$, Table 2) content by 0.55 ± 0.01 m, and increases sea ice melt by 0.57 ± 0.03 m, indicating that $>92\%$ of the meteoric water column inventory consists of GMW (Appendix A5). A substantial fraction of local (and non-local) precipitation will be deposited on sea-ice, much of which is subsequently advected out of the study area (Assmann et al., 2005), and as a result have no impact on locally measured meteoric water content, suggesting that GMW could comprise an even greater fraction.

455 While previous studies (Biddle et al., 2019; Meredith et al., 2010) have excluded the upper water column from GMW accounting, due to uncertainty surrounding the impact of local precipitation, our results suggest realistic (glacial) meteoric water content can still be estimated in the upper water column. Nearly half (~ 4 m) of the water column meteoric water content resides in the upper 200 m, and $>92\%$ of water column meteoric water is comprised of glacial meltwater (Appendix A5). Discounting

460 this upper water column meteoric water unnecessarily hampers the usage of this technique for glacial meltwater accounting. The potential for overestimating (glacial) meteoric water due to precipitation is dwarfed by the potential for underestimating glacial meltwater content by excluding the upper water column.

4.3 Temporal changes in mean meteoric water column inventories

465 We have estimate average meteoric water column inventories in the SE Amundsen Sea using seawater oxygen isotopes and salinity in a three-endmember mixing model. In 1994, 2007, 2014, and 2020, there is a tendency for the maximum integrated meteoric water volume to extend westward from the SW corner of the PIIS, and along the eastern TIS (Figure 1), consistent with the gyre-like circulation there (Thurnherr et al., 2014). This pattern of meteoric water distribution is consistent with local GMW
470 patterns previously observed using traditional hydrographic tracers (Thurnherr et al., 2014; Naveira Garabato et al., 2017; Wåhlin et al., 2021).

Local meteoric water content varies from a low of 7.6 ± 0.5 m in 1994 to highs of 9.2 ± 0.6 m in 2000 and 2020. Inventories fluctuated over the latter period, without apparent trend, dependent on the spatial and
475 temporal coverage of available datasets. While salinity and $\delta^{18}\text{O}$ alone cannot be used to determine basal melt rates, the average meteoric water inventories are sufficient to identify relatively small changes in melt rates, assuming a constant residence time. The inventories are consistent with other studies suggesting relative stability in recent decade-scale glacial melt rates with significant interannual variability (Paolo et al., 2018; Dotto et al., 2019; Adusumilli et al., 2020; Flexas et al., 2022). A recent
480 modelling study shows an increase in basal melt through the 1990s, followed by relative stability from 2000-2020 (Flexas et al., 2022).

The mCDW entering the SE Amundsen Sea and accessing the underside of the ice shelves has been shown to exhibit little seasonal variability, with a maximum variance in T of $<0.1^\circ\text{C}$, salinity of <0.05 g/kg, and thickness of <50 m (Mallett et al., 2018). All samples used in this study were collected from
485 12 January to 15 March, while melt rates for the PIIS and TIS exhibit very little seasonal variability (Kimura et al., 2017). With a residence time of ~ 2 years (Tamsitt et al., 2021), it is unlikely that the variability in yearly meteoric water column inventories is a product of a seasonal signal.

490 Glacial meltwater measured in the SE Amundsen Sea includes mCDW-driven basal melt, local iceberg melt, and meltwater entering the ocean at the grounding zone that is driven by the geothermal heat flux to the base of the ice sheet (~ 5.3 Gt/y; Joughin et al., 2009). The greatest uncertainty in using average meteoric water inventories as a means for GMW accounting arises from the poorly constrained residence time of regional shelf waters, as there has been little study of this component. With local
495 circulation generally moving waters westward (Nakayama et al., 2013; Thurnherr et al., 2014; Naveira Garabato et al., 2017; Nakayama et al., 2019; Wåhlin et al., 2021), it is likely that the calculated meteoric water fractions in the study area (with the exception of those on the western side of TIS) are primarily comprised of basal melt from PIIS.

500 Assuming a mean residence time of 2 years (Tamsitt et al., 2021) and GMW comprising >92% of total
meteoric water column content (Appendix Error! Reference source not found.) is representative of the
whole study area (~30,000 km² ocean), we estimate GMW inputs of between 106±17 Gt/y in 1994 to
129±17 Gt/y in 2000/2020. Though empirical, these figures are consistent with satellite-based estimates
505 of mass loss from PIIS via basal melt (Rignot et al., 2013, 2019a), demonstrating the utility of
geochemical ocean measurements for estimating ice shelf melt rates.
to the mCDW endmember, which comprises >95% of the mixture at any given location.

4 Discussion

In this study, we estimate average water column Glacial Meltwater in the SE Amundsen Sea using
seawater oxygen isotopes and salinity in a three-endmember mixing model. We defined mCDW and
510 GMW signatures separately for each data year and compare GMW fractions rather than $\delta^{18}\text{O}$ values.
This this limits way any systematic isotopic offsets between laboratories from affecting the year's
calculated GMW fractions (Appendix A2). The results of this study show local meltwater content
varying from a low of 7.6 m in 1994 to a high of 9.2 m in 2020. Between 2000–2020, inventories
515 fluctuate, without an apparent trend. Several other studies have also shown relatively stable basal melt
rates, fluctuating interannually in this region of Antarctica (Paolo et al., 2018; Holland et al., 2019;
Adusumilli et al., 2020; Flexas et al., 2022).

Basal melt in the Amundsen Sea sector is driven by the thickness of the mCDW layer transported on-
shore, rather than its temperature (Dutrieux et al., 2014; Jenkins et al., 2018). The thickness of the
520 mCDW layer is controlled by local wind forcing of a shelf break undercurrent, coupled to the
Amundsen Sea Low. Changes in local wind forcing have decelerated the local undercurrent, decreasing
the thickness of the mCDW layer and reducing the heat transport onto the shelf and resulting in an
overall cooling of Amundsen Sea shelf waters from 2010 through 2016 (Dutrieux et al., 2014; Webber
et al., 2017; Jenkins et al., 2018; Dotto et al., 2020). Grounding line retreat of PHS and TWG had been
525 accelerating, but experienced a slowdown between 2010–2015 relative to the preceding period driven by
changes to offshore winds (Christie et al., 2023). Our inventories show a local high in 2000, and a local
low in from 2009–2019. A recent modelling study showed an increase in PHS and TWG basal melt
between the early 1990s and 2000, followed by relative stability thereafter (Flexas et al., 2022). Our
530 results show an increase in average GMW after 1994, followed by interannual fluctuation from 2000–
2020, with average GMW inventories remaining well above 1994 levels. Assuming steady-state ocean
circulation strength, the relatively steady GMW inventories are consistent with the linear, longer-term
freshening trend reported downstream in the Ross Sea (Jacobs et al., 2022).

We calculate average GMW inventories from the surface to 800 m. In most years, there is a tendency
535 for the maximum integrated GMW volume to extend westward from the SW corner of the PHS, and
along the Thwaites Glacier Tongue (TGT), consistent with the gyre-like circulation in the area between
PHS and TGT. This pattern of GMW distribution is consistent with that previously observed using

540 traditional hydrographic tracers (Naveira-Garabato et al., 2017). Roughly half of the total meltwater inventory is in the upper 200 m, and inventories below that depth yield the same general trend in interannual variability (Appendix A5), indicating that the observed variability is indeed indicative of basal melt, and not merely an artefact of local interannual variability in precipitation. A spatial sensitivity analysis also shows no significant impact of year-to-year variation in sampling locations on average GMW inventory (Appendix A4).

545 The Amundsen Sea sector receives 0.5 m–1 m (water equivalent) of precipitation each year (Donat-Magnin et al., 2021) and the residence time of deep shelf waters in this region is ~one year (Tamsitt et al., 2021). With a local precipitation $\delta^{18}\text{O}$ of -15‰, even an entire year's precipitation remaining in the upper water column at the time of sampling would only account for ~3%–7% of the overall column inventories (Appendix A5). Furthermore, a substantial fraction of local precipitation will be deposited on sea ice, much of which is subsequently advected out of the study area (Assmann et al., 2005). While previous studies (Biddle et al., 2019; Meredith et al., 2010) have excluded the upper water column due to uncertainty surrounding local precipitation, our results suggest realistic glacial meltwater content can still be estimated in near-surface seawater.

5 Conclusion

555 We ~~use used a time-series of~~ seawater $\delta^{18}\text{O}$ and salinity ~~data~~ collected in the SE Amundsen Sea from 1994 to 2020, ~~using salinity and $\delta^{18}\text{O}$ to calculate water column inventories of meteoric (fresh) water through the GMW. The average water column. Freshwater intercepts from $\delta^{18}\text{O}$ -salinity plots produce a well-constrained meteoric water endmember consistent inventory of GMW was lowest in 1994 and highest in 2000 and 2020, with measurements from regional ice cores, and indicative of glacial enough uncertainty in meltwater. While limited by sampling years and number of observations, meteoric water (which we estimate inventories and interannual variability to be >92% GMW) measured in 1994 is lower than measurements made from 2000-2020, where meteoric water content averaged $8.9 \pm 0.3\text{m}$, with a maximum difference of 0.75m. linear increase of 0.02 m/y statistically insignificant. These results are consistent with recent studies showing an increase in basal melt through the 1990s, followed by relative stability and interannual variability from 2000 through in basal melt rates in this region. Our results also suggest a lower melt period through the 2000s, followed by the highest melt year in 2020. A linear increase of $0.03 \pm 0.02\text{ m/y}$ over the study period is insignificant, with interannual variability that is larger than the increasing trend in meteoric water content.~~

570 The WAIS is an important region for understanding ~~future global~~ sea level rise, ~~as changes in winds and particularly with increasing ocean circulation can increase temperatures driving basal melting of ice shelves, melt and increasing the flow of their ice streams into the sea. Changes in meteoric water inventories in the SE Amundsen Sea study region. More recent remote sensing and modelling studies are consistent with satellite-based estimates of annual mass loss from the PIIS, more indicative of interannual variability than acceleration in WAIS melt. The meltwater inventories calculated here from seawater $\delta^{18}\text{O}$ observations also suggests a relatively stable basal melt rate in the SE Amundsen Sea,~~

580 ~~with interannual fluctuations potentially masking an increase over 2.6 decades.~~ These results
demonstrate the ~~independent~~ utility of seawater $\delta^{18}\text{O}$ and salinity data as an independent method for
estimating ice shelf basal melt rates. Regular sampling for $\delta^{18}\text{O}$ in monitoring and helping to better
585 ~~constrain satellite-based estimates of basal melt and~~ salinity in this region could reveal if the existing
record and its variability will extend into an era when ice shelves are likely to be thinner, with their
grounding lines deeper and farther south.~~glacial change.~~ Integration of $\delta^{18}\text{O}$ data into numerical models
could also~~should~~ further our understanding of ocean circulation ~~strength~~ and ice loss along this
climatically sensitive sector of the WAIS. ~~Continued sampling for $\delta^{18}\text{O}$ in this region could also reveal~~
~~if and when our measured rates of meltwater volume, already consistent with downstream freshening,~~
~~rise significantly above the observed short-term variability.~~

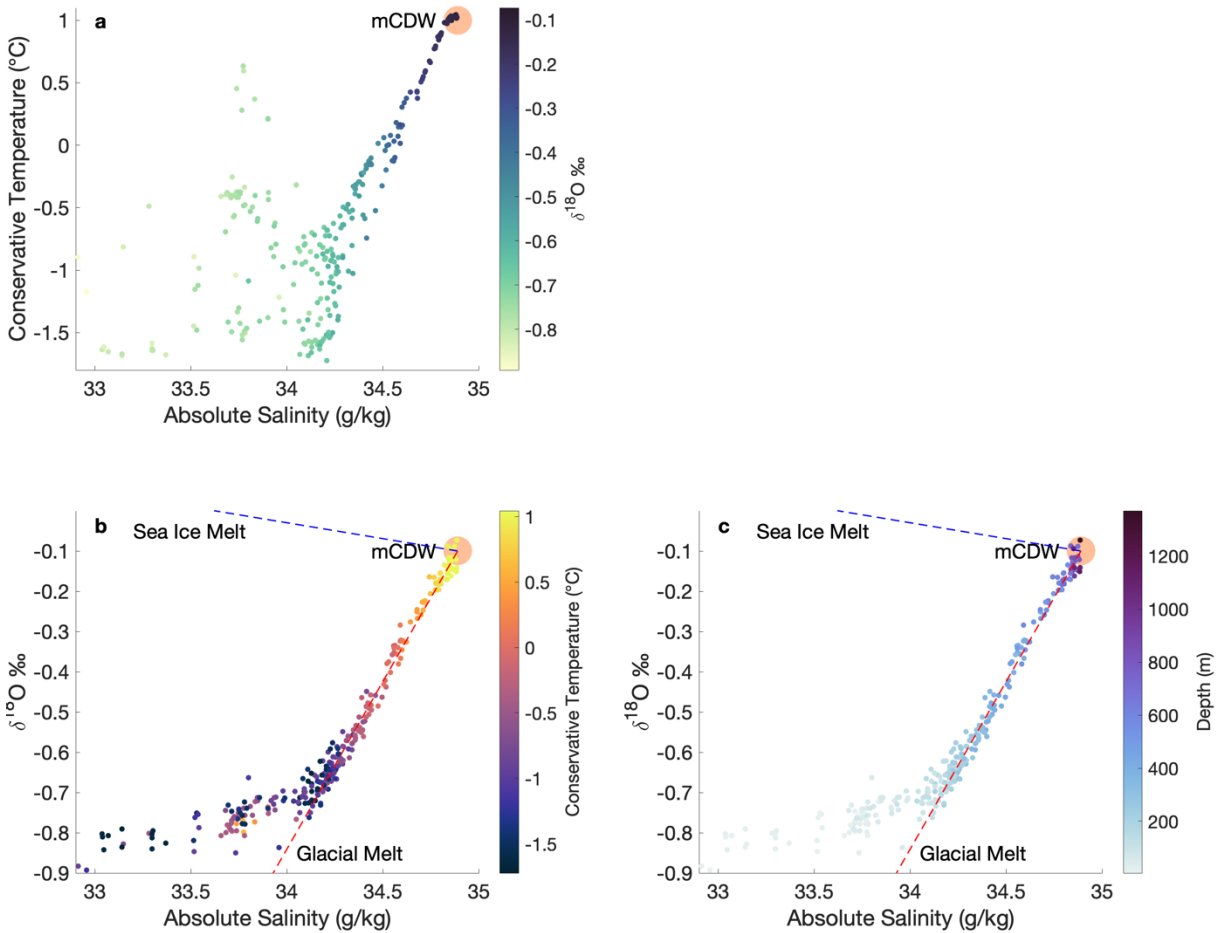
APPENDIX

590 A1 Defining mCDW

Modified Circumpolar Deep Water (mCDW) is one of three endmember waters ~~we useused~~ in a mixing model to determine glacial meltwater fractions. As the salinity and $\delta^{18}\text{O}$ of mCDW are well observationally well constrained, ~~with-and-display~~ interannual variability ~~and, mCDW~~ properties ~~that~~ are defined separately for each year, ~~as in: Figure A1 with 2020 data. Error! Reference source not~~ 595 ~~found. illustrates that process, using 2020 data.~~ Being the warmest, saltiest water on the continental shelf, mCDW appears at the top-right on a T-S diagram (Panel a), where it also identifies waters that are ~~the~~ least-depleted in $\delta^{18}\text{O}$.

In ~~Panels~~Panel b and c, the same ~~2020~~ data ~~showare plotted, with~~ the keystone positions of mCDW in ~~axis showing $\delta^{18}\text{O}$, and the colors indicating~~ temperature/salinity/ $\delta^{18}\text{O}$ /depth space. The red and (blue) 600 dashed lines show property ~~mixingmixng~~ lines between mCDW, ~~and~~ glacial meltwater (GMW) ~~and~~ sea ice melt, with the colder waters being fresher and more depleted ~~in $\delta^{18}\text{O}$.~~

~~Panel c covers the same dataset, but with colors illustrating depth.~~ Most data ~~are lie~~ above ~~~800 m~~800m, 605 with the least $\delta^{18}\text{O}$ depletion in a few ~~deepdeeper~~ depressions. Waters ~~that fallare diverted~~ off the mCDW-GMW mixing line in the upper ~~200m have been~~200 m of the water column, influenced by sea ice melting/~~formation~~ and atmospheric processes. Sea ice melt ~~will freshen saltier waters but~~ has a slightly positive (+2.1‰) $\delta^{18}\text{O}$, while GMW has a very negative (~~~-30‰~~) $\delta^{18}\text{O}$. ~~Both freshen seawater, with the sea ice melt slightly counterbalancing~~ $\delta^{18}\text{O}$ (~~~-29‰~~). ~~Its influence makes resultant mixtures~~ 610 ~~fresher, but somewhat counterbalancees~~ the strong negative $\delta^{18}\text{O}$ of GMW.



615 **Figure A1: Temperature, salinity, and $\delta^{18}\text{O}$ and depth from 2020 data.** **A)** T-S diagram with colorbar showing $\delta^{18}\text{O}$. **b)** $\delta^{18}\text{O}$ vs salinity with colorbar showing temperature. **C)** $\delta^{18}\text{O}$ vs salinity with colorbar showing sample depth. **The most saline samples are also the warmest, deepest, and least depleted in $\delta^{18}\text{O}$.** Data **diverged** from the mCDW-glacial melt mixing line at depths shallower than 200 m due to the presence of sea ice melt in the admixture. In Panels b and c, dashed lines show the associated property mixing lines for mCDW mixing with sea ice melt, or GMW.

620 In **Figure 2** of the main text, $\delta^{18}\text{O}$ -salinity plots for each year reveal several data points near the ~~the~~ salinity maximum, with some variability in the corresponding $\delta^{18}\text{O}$. ~~Below~~ **Using only data from below 200 m**, trendlines ~~that are~~ extrapolated to **zero**-salinity intercepts define the mCDW and **meteoric water (GMW)** endmembers used in the mixing model. mCDW and **meteoric water** ~~GMW~~ $\delta^{18}\text{O}$ are defined ~~at~~ **as the δ salinity maximum and θ -salinity zero-salinity intercepts of the trendlines intercept on the trendline, respectively (Table 2 Table 2)**. The **mCDW** location ~~of mCDW~~ corresponds to conventional measures of the deepest and warmest waters on the **continental** shelf. The calculated **zero**-salinity intercept values are consistent with the properties of **locally available** ~~local~~ GMW.

625

A2 Inter-laboratory offsets

630 $\delta^{18}\text{O}$ When using data from produced by different laboratories are subject, it is important to possible be aware of the potential for systematic offsets. For example, a $\sim 0.1\text{‰}$ $\delta^{18}\text{O}$ offset between the 2014 data and other years (Figure A2) is likely the result of an inter-laboratory calibration offset. On the other hand, greater scatter in the 2009 data suggests that evaporation during sample storage left some samples less depleted in $\delta^{18}\text{O}$. Here, we primarily compare have compared calculated meteoric water fractions rather than $\delta^{18}\text{O}$ values, with mCDW and meteoric waterGMW signatures defined separately for each year so that any offset will not affect the values of samples from that year relative to their mCDW/meteoric waterGMW signatures.

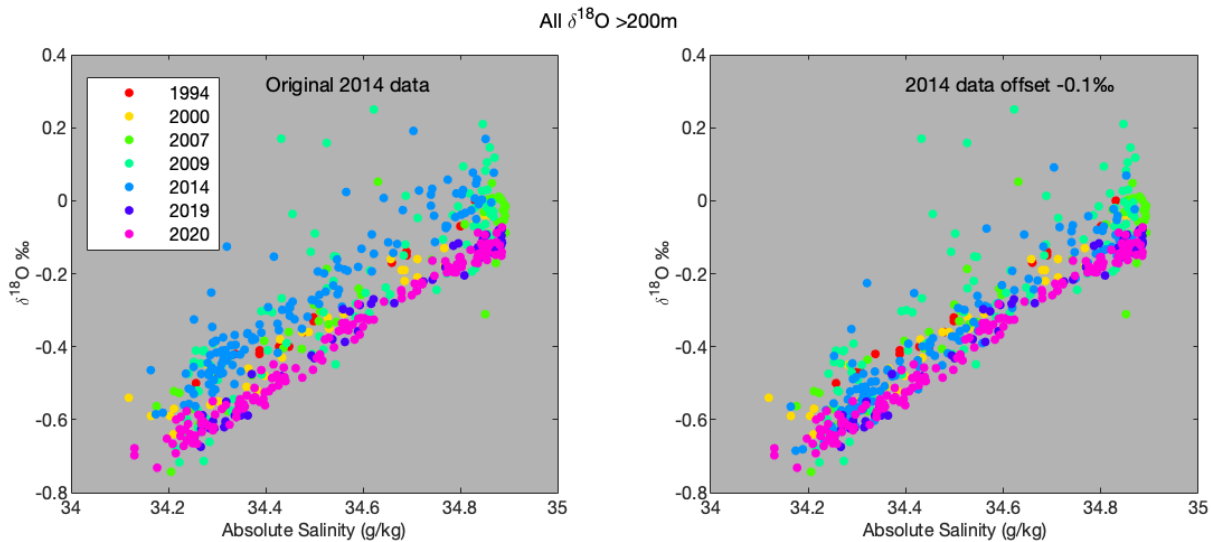


Figure A2: $\delta^{18}\text{O}$ vs Absolute salinity for all years, from data >200 m. Left panel: All $\delta^{18}\text{O}$ vs salinity data, with the 2014 data as published in (Biddle et al., 2019). Right panel: same, with a -0.1‰ offset correction applied to the 2014 data.

640 -A sensitivity analysis, wherein all sample data from a given year were offset, and mCDW/meteoric waterGMW signatures were re-calculated using the offset data. The result offset data and endmembers endmembers were used to calculate meteoric waterGMW fractions in the 3-endmember mixing model, with— sea ice melt values remaining remained static. We found that an inter-lab offset of

645 5.7‰ $\delta^{18}\text{O}$ (Figure A3) would be necessary to change the calculated meteoric waterGMW fraction by an amount greater than the analytical precision ($\pm 0.04\text{‰}$ $\delta^{18}\text{O}$, ± 0.003 g/kg for absolute salinity) and environmental uncertainty based on ice core measurements ($\pm 1.9\text{‰}$ for $\delta^{18}\text{O}$). Inter-associated with the calculation (± 1.6 g/kg). Since, inter-lab offsets should be less would not be expected to be greater than 0.1‰ (Walker et al., 2016), so

650 any offsets will would not be significant when comparing calculated meteoric water fractions.

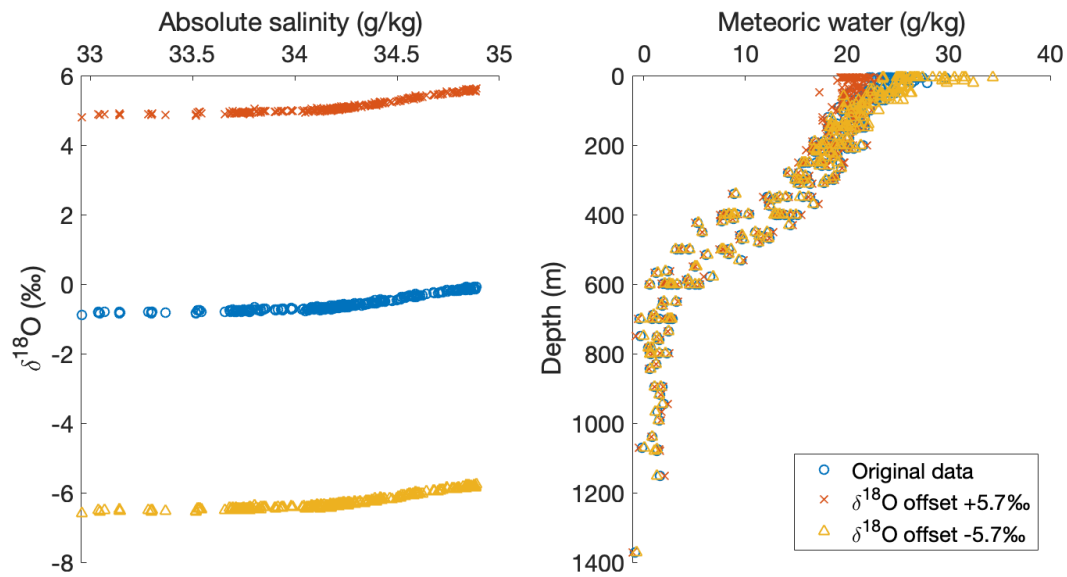


Figure A3: Impact on inter-lab offsets on calculated meteoric (glacial melt) water fraction for NBP20-02 data. The left panel shows the $\delta^{18}\text{O}$ offset ($\pm 5.7\text{‰}$) necessary to significantly affect calculated meteoric water fractions, when using mCDW and meteoric water endmembers calculated from that data. The right panel shows the calculated meteoric water fractions produced using the original, and offset data. The calculated meteoric water fractions are impacted very little because two of the three endmembers (mCDW and meteoric water) are defined by the offset data.

655

660 A3 Uncertainty in calculated ~~meteoric~~ water fractions

665 ~~Since meltwater fractions are calculated using analytical measures of salinity and $\delta^{18}\text{O}$, the accuracy and precision of these measurements are important. CTD salinity sensors have a reported precision of ± 0.002 . The Isotope Ratio Mass Spectrometer (IRMS; 1994 to 2014) measurements have a measured precision of $\pm 0.04\text{‰}$ based on replicates, while the Cavity Ring-Down Mass Spectrometer (CRDS) achieved a precision of $\pm 0.02\text{‰}$. The meteoric (GMW) endmember is arguably the least-well constrained, with glacial ice in West Antarctica ranging from -20‰ to -40‰ , but much of that uncertainty has been eliminated by using the zero-salinity intercept determination on a $\delta^{18}\text{O}$ -salinity mixing line, corroborated by nearby ice core values as discussed in the main manuscript. mCDW is well-constrained, based on many accurate in-situ measurements. Our sea ice melt endmember is adopted from previously published studies in the region (Meredith et al., 2008, 2010, 2013; Randall-Goodwin et al., 2015; Biddle et al., 2019).~~ Since meltwater fractions are calculated using analytically-derived measures of salinity and $\delta^{18}\text{O}$, the accuracy and precision of these measurements are important. CTD salinity sensors have a reported precision of ± 0.002 . The IRMS (1994 to 2014) measurements in this study have a reported precision of $\pm 0.04\text{‰}$ based on replicates, while the CRDS achieved a precision of $\pm 0.02\text{‰}$. Our end-member values for sea ice melt and meteoric water are largely theoretical. The meteoric endmember is arguably the least-well constrained, with glacial ice in West Antarctica ranging from -20‰ to -40‰ , but much of that uncertainty has been eliminated by using the θ -salinity intercept determination on a $\delta^{18}\text{O}$ -salinity mixing line, corroborated by nearby ice core values, as discussed in the main manuscript. mCDW is the best constrained endmember and is based on many in-situ measurements.

We use Monte Carlo simulations to estimate uncertainty in ~~our~~ water mass fraction calculations. We ran 10,000 simulations with input values varied randomly within these bounds and represent uncertainty by the standard deviation of the difference between the simulated ~~runs~~, and ~~the~~ initial runs.

685 ~~Observations~~run. Each parameter ($\delta^{18}\text{O}$, salinity) was varied around the reported endpoints (**Table 2**) and the measured observational values for each of our samples, by the uncertainty associated with environmental variability, and instrument precision (**Table A1**). All observations were varied randomly perturbed by analytical precision above, (0.04‰ $\delta^{18}\text{O}$; 0.002 g/kg salinity); these perturbations also impacting have an impact the mCDW and meteoric waterGMW endmembers for each run. Additional perturbations, since they are calculated from observations >200 m. In addition to perturbations made to the endmember values; sea ice melt based on theoretical values (Rohling, 2013), meteoric water by observations, endmembers are further perturbed. The perturbation used for the glacial meltwater endmember is the standard deviation of the ITASE01-2 ice core. The perturbations for sea ice melt were selected based on theoretical values (Rohling, 2013). mCDW salinity perturbations were selected based on the data distribution for each year. $\delta^{18}\text{O}$ was varied by the results of a spatial sensitivity analysis (**Appendix A4.2**) and $\delta^{18}\text{O}$ was varied by half standard deviation associated with the 95% prediction interval ($\sim 1\sigma$) of produced from the >200 m $\delta^{18}\text{O}$ -salinity relationship at the salinity

maximum. Perturbations used in the uncertainty analysis are summarized in **Table A1**; salinity was varied by the standard deviation in salinity of the highest $\delta^{18}\text{O}$ data falling within the 95% prediction interval at the salinity maximum.

Table A1: Perturbations for uncertainty analysis. Perturbations are based on analytical precision for observations, the ITASE01-2 ice core for meteoric water, and theoretical values for sea ice melt (Rohling, 2013). mCDW perturbations are based on the 95% prediction interval of the >200m $\delta^{18}\text{O}$ -salinity relationship at the salinity maximum, and salinity perturbations are based on the results of the spatial randomization analysis (Appendix A4.2). **Endmember perturbations for uncertainty analysis**

Parameter	Absolute Salinity perturbation (g/kg) (‰)	$\delta^{18}\text{O}$ Absolute Salinity perturbation (‰) (g/kg)
Observations	0.002	0.04 (0.02 for CRDS)
Meteoric water	N/A	1.9
Glacial meltwater (meteoric)	1.9	N/A
Sea ice melt	2	0.1
mCDW, 1994	0.010*	0.010
mCDW, 2000	0.011	0.012
mCDW, 2007	0.009	0.018
mCDW, 2009	0.002	0.021
mCDW, 2014	0.015	0.017
mCDW, 2019	0.006	0.006
mCDW, 2020	0.017	0.004

* For 1994, we perturbed salinity by the average salinity standard deviation for the other years, to compensate for the smaller number of samples

The mean uncertainty in meteoric associated with GMW water fractions ranges from ± 1.1 g/kg in 2019 to ± 1.7 g/kg in 2009, this corresponding to ± 0.5 – 0.7 m average meteoric water column inventories uncertainty between ± 0.5 m in 2019 inventory. GMW and ± 0.7 m in 2009 (Table 3). Meteoric water and sea ice melt Sea Ice Melt fractions vary inversely, while mCDW fractions remain relatively stable. Calculations are most impacted by changes to the mCDW endpoint, as mCDW makes up ~ 99 – 95 % of the (800m) water column on average; >95 % in the meteoric water and sea ice melt rich surface waters, and >98 % at all depths below 200 many given location.

For a small number of samples from 2007 (3), 2009 (9), and 2014 (2) suggest negative meteoric water the calculated GMW fractions, nine beyond are negative. For the 3 samples in 2007, and 2 in 2009, these figures are within the uncertainty described above. The negative meteoric water GMW fractions result from when high-salinity deep waters with were measured to have a $\delta^{18}\text{O}$ values significantly less negative than the mCDW endpoint in the 3-endmember mixing model, reflective of uncertainty in the data and/or model limitations. Those years also display a used in the GMW calculation. The spatial variability in mCDW, is reasonably well constrained year to year, with a wider spread in mCDW $\delta^{18}\text{O}$ for 2007, 2009, and 2014 than in other years, likely due. The samples in question may have been subject to evaporation during, resulting in a higher $\delta^{18}\text{O}$, highlighting the importance of appropriate sample collection and storage.

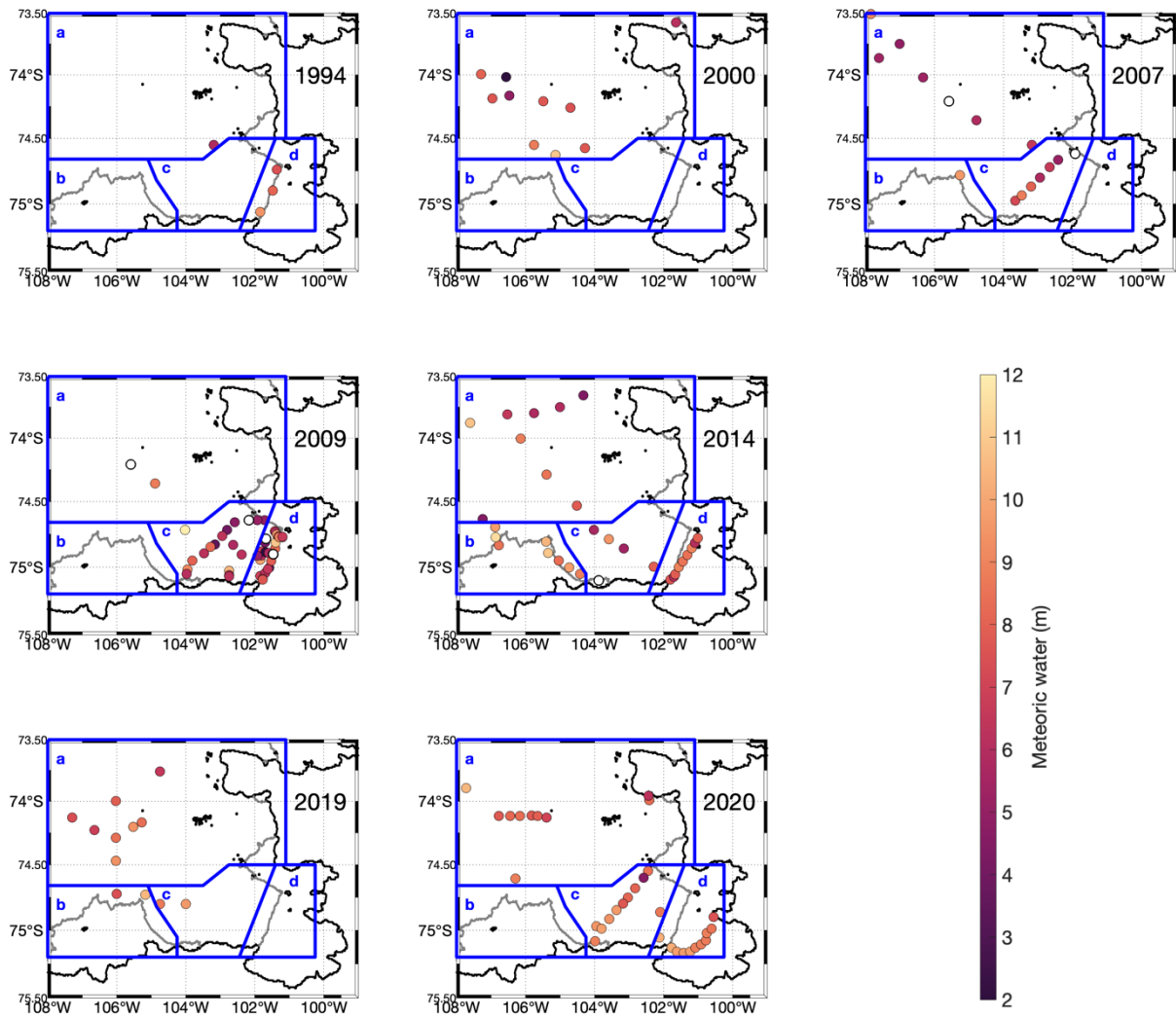
Sea ice melt and mCDW fractions are discussed in **Appendix A6**.

730

A4 Geographical sensitivity of endmembers and meteoric water column inventories mCDW signature and meltwater inventory

A4.1 Geographic clustering analysis

735 We analyzed the spatial sensitivity of results by splitting the study area into four groups and analyzing data from those groups for each year (Figure A4, Table A2). For each area, mCDW and meteoric water endmembers were defined based on only those data. In 10,000 Monte Carlo simulations, the observations and endpoints were perturbed by uncertainty associated with analytical precision and environmental variability (Table A1).



740

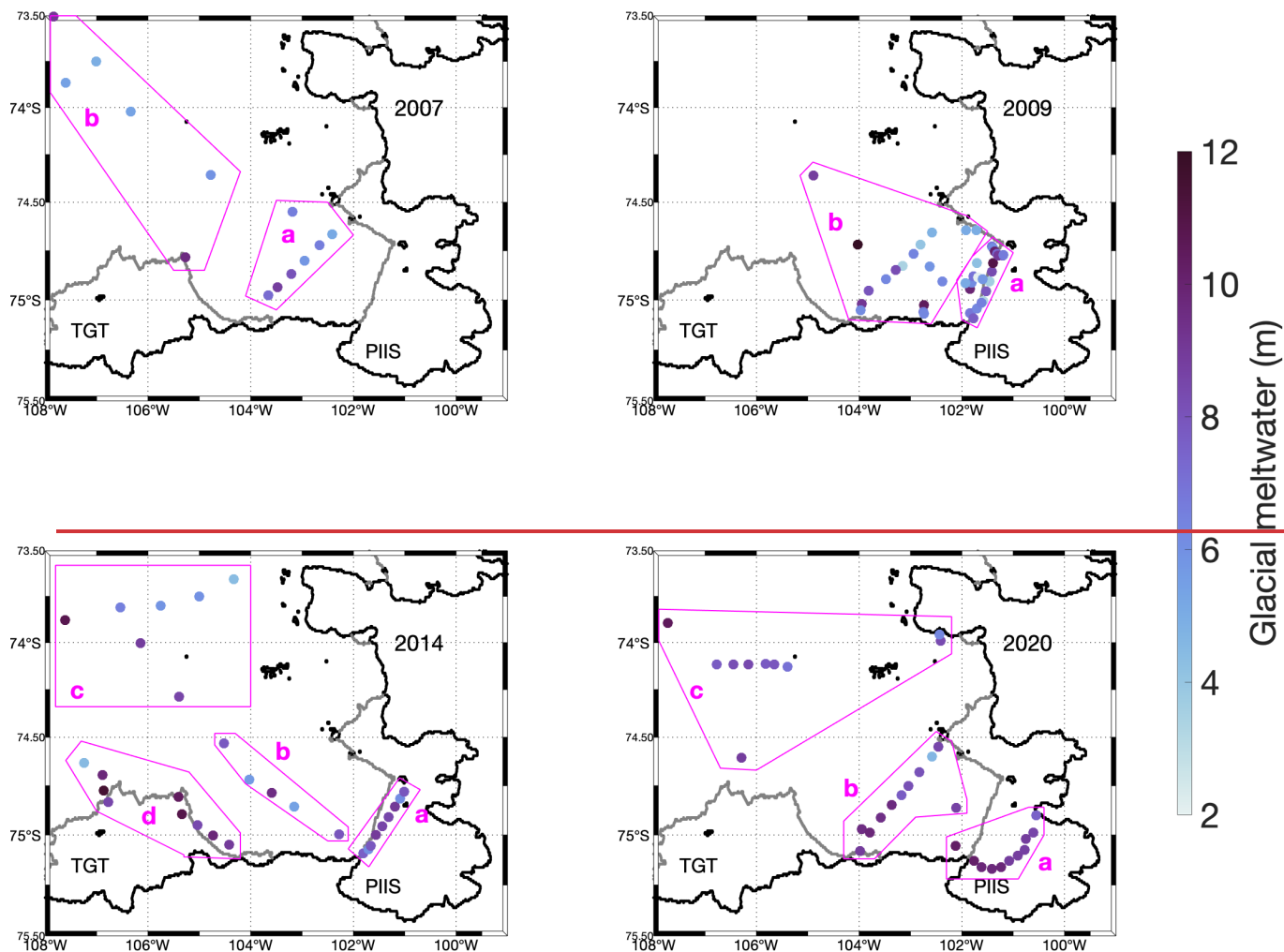


Figure A4: Sampling locations and geographic group boundaries for all years. Dot colors show meteoric water column inventory at individual stations, and outlines showing geographic groupings of stations for geographic sensitivity analysis (Table A2). Some locations provided only partial column inventories. **Sampling locations for 4 years and analyzed data groupings.** To understand how much year-to-year differences in sampling location affects mCDW and GMW fingerprinting, and average meltwater inventory calculations, we selected the 4 years with the greatest number of data points and ran these analyses on different geographic groupings of sample data (Table A2).

745

Table A2: Results of geographic grouping sensitivity analysis. mCDW is defined as the $\delta^{18}\text{O}$ value at the salinity maximum falling on the linear regression of all salinity- $\delta^{18}\text{O}$ measurements deeper than 200m in each group of stations; meteoric water $\delta^{18}\text{O}$ is defined as the 0 salinity zero-salinity intercept on that same line. Uncertainty in mCDW $\delta^{18}\text{O}$ is represented by half the 95% prediction interval at the salinity maximum ($\sim 1\sigma$), and uncertainty in salinity is the result of the randomization spatial sensitivity analysis, plus variation from perturbation of observations (Appendix A4.2), manufacturer's stated analytical precision. Average meteoric water inventory is the depth integration of the Gaussian fit of all calculated meteoric water fractions within each group, with uncertainty represented as the standard deviation in meteoric water fractions achieved using 10,000 Monte Carlo simulations perturbing the observations and endpoints by associated analytical and environmental uncertainty (Table A1). For each group of stations, mCDW and meteoric water endmembers used in meteoric water calculations are defined using only those data.

Year	Group	# of Stations	# of samples	mCDW absolute salinity (g/kg)	mCDW $\delta^{18}\text{O}$ (‰ vs VSMOW)	Meteoric water $\delta^{18}\text{O}$ (‰ vs VSMOW)	Average meteoric water column inventory (m)	Meteoric water fraction uncertainty (g/kg)
1994	a	1	8	34.83±0.010	-0.02±0.02	-31.9±3.0	6.3±0.5	1.3
	d	3	18	34.86±0.010	-0.02±0.01	-28.3±2.0	8.0±0.6	1.6
2000	a	10	62	34.88±0.012	-0.05±0.01	-28.7±0.9	9.2±0.7	1.7
2007	a	8	34	34.90±0.009	-0.04±0.02	-26.1±1.4	8.4±0.8	1.8
	b	1	4	34.85±0.009	-0.05±0.63	-29.7±2.7	10.3±0.8	1.5
	c	6	36	34.87±0.010	0.01±0.04	-32.1±1.4	9.0±0.7	1.6
2009	a	2	4	34.87±0.003	0.01±0.7	-43.7±4.8	7.0±0.6	1.1
	c	18	61	34.87±0.003	-0.01±0.04	-28.8±1.1	8.7±0.8	1.8
	d	26	110	34.87±0.002	0.02±0.03	-29.0±0.7	8.5±0.7	1.7
2014	a	9	57	34.86±0.015	0.04±0.03	-27.2±1.2	8.3±0.6	1.8
	b	8	61	34.87±0.015	0.07±0.02	-32.1±1.0	10.1±0.7	1.5
	c	5	19	34.83±0.015	0.06±0.02	-33.6±2.0	7.9±0.5	1.4
	d	9	76	34.83±0.015	0.06±0.02	-31.7±1.1	7.5±0.5	1.4
2019	a	8	68	34.89±0.006	-0.1±0.01	-27.6±0.6	8.2±0.6	1.2
	b	2	21	34.87±0.006	-0.12±0.01	-30.6±0.8	10.0±0.7	1.1
	c	2	18	34.85±0.006	-0.11±0.02	-31.5±1.0	8.2±0.5	0.9
2020	a	10	90	34.89±0.016	-0.11±0.01	-28.2±0.4	8.7±0.6	1.3
	c	11	70	34.86±0.017	-0.12±0.01	-29.6±0.5	8.7±0.5	1.2
	d	11	120	34.85±0.017	-0.13±0.0	-29.7±0.4	8.5±0.5	1.1

mCDW (as defined in Appendix A1) was broadly shows little geographic sensitivity. In all years, salinity varied by less than observed seasonal salinity variation in mCDW (0.01 g/kg; Mallett et al., 2018). mCDW $\delta^{18}\text{O}$ exhibited less variation than that associated with instrumental precision.

The meteoric water $\delta^{18}\text{O}$ fingerprint calculated for different geographic groupings each year is not geographically sensitive – as would be expected with deep meteoric water (basal meltwater) having a single source. 2009 Group a rendered a significantly different meteoric water endmember, however this number is based on data from just 4 samples (3 from >200 m); given the data limitations and the sample quality issues for 2009, it is unlikely that the -43.7±4.8‰ endmember is representative.

In general, the meteoric water column inventories appear insensitive to geographic groupings. The exceptions are Group a in 1994 and 2009, and Group b in 2007, 2014, 2019. In 1994, Group a contains

only a single station in 1994 (8 samples), and only 4 samples (2 stations) in 2009. Group b consists of those samples collected alongside TIS; locations likely to be dominated by meltwater originating from beneath PIIS (Wåhlin et al., 2021). Surprisingly, given the small number of samples collected near TIS in 2007 and 2019, the meteoric water inventories from Group b stations are consistent.

775 A4.2 Spatial randomization analysis

A geographic sensitivity Monte Carlo analysis involved calculating results from random sets of 3 stations 10,000 times (Table A3). For each group of 3 stations, mCDW and meteoric water endmembers, and average meteoric water column inventories were calculated using only those data. Stations with fewer than 2 samples >200 m were excluded. As the 3-endmember mixing model is most
 780 sensitive to the mCDW endmember, a set of stations lacking samples >800m (deeper than the sub-cavity ridge; ‘pure’ mCDW) had a random mCDW sample from >800m that year added to the data set for analysis.

785 **Table A3: Results of station randomization sensitivity analysis.** mCDW is defined as the $\delta^{18}\text{O}$ value at the salinity maximum on the linear regression of all salinity- $\delta^{18}\text{O}$ measurements deeper than 200 m in each group of stations; meteoric water $\delta^{18}\text{O}$ is defined as the zero-salinity intercept on that same line. Average meteoric water inventory is the depth integration of the Gaussian fit of all calculated meteoric water fractions within each group. In all cases, uncertainty is represented by the standard deviation in the results obtained across 10,000 Monte Carlo simulations for each year. 1994 had only 4 stations, variability represented by this analysis for that year may be artificially low.

<u>YEAR</u>	<u>Mean mCDW salinity (g/kg)</u>	<u>Mean mCDW $\delta^{18}\text{O}$ (‰)</u>	<u>Mean meteoric water $\delta^{18}\text{O}$ (‰)</u>	<u>Mean meteoric water inventory (m)</u>	<u>% Meteoric water inventory uncertainty</u>	<u>Meteoric water fraction uncertainty (g/kg)</u>
<u>1994*</u>	<u>34.86±0</u>	<u>-0.01±0.01</u>	<u>-29.4±0.6</u>	<u>7.6±0.2</u>	<u>2.9%</u>	<u>0.1</u>
<u>2000</u>	<u>34.87±0.03</u>	<u>-0.06±0.03</u>	<u>-28.7±1.6</u>	<u>8.8±0.5</u>	<u>5.4%</u>	<u>0.8</u>
<u>2007</u>	<u>34.89±0.01</u>	<u>-0.03±0.04</u>	<u>-27.9±3.4</u>	<u>9.0±0.7</u>	<u>7.3%</u>	<u>1.1</u>
<u>2009</u>	<u>34.86±0.06</u>	<u>-0.01±0.08</u>	<u>-28.7±4.1</u>	<u>8.8±0.7</u>	<u>8.0%</u>	<u>1.8</u>
<u>2014</u>	<u>34.84±0.03</u>	<u>0.05±0.05</u>	<u>-31.1±3.3</u>	<u>8.5±0.8</u>	<u>9.4%</u>	<u>1.1</u>
<u>2019</u>	<u>34.88±0.01</u>	<u>-0.10±0.01</u>	<u>-29.6±1.6</u>	<u>8.5±0.4</u>	<u>4.9%</u>	<u>0.6</u>
<u>2020</u>	<u>34.87±0.02</u>	<u>-0.11±0.02</u>	<u>-29.1±1.4</u>	<u>8.8±0.6</u>	<u>6.3%</u>	<u>0.7</u>

790 The mCDW properties appear geographically insensitive, though 2009 and 2014 exhibit higher variability than other years, potentially due to sample collection and/or storage issues (Appendix A2, A7).

795 Meteoric water endmember properties showed greater spatial variability in 2007, 2009, 2014. In these 3 years, the data show the greatest scatter, and station locations do not always have mCDW samples near the seafloor. The lengthy meteoric water endmember extrapolation benefits from many samples collected below 200 m.

800 The impact of sample geographic location variability is generally comparable to that of the primary
uncertainty analysis (analytical precision and environmental variability), with the exceptions of 2009
and 2014. However, the 2014, spatial uncertainty is somewhat inflated due to the very high (>10m)
meteoric water inventories at stations immediately alongside TIS, while the 2009 data are impacted by
sample storage issues, and poor depth resolution at some locations.

805

mCDW $\delta^{18}\text{O}$ (as defined in Section A1, above) was shown to not be geographically sensitive. Surprisingly, in 2007, mCDW defined using only the stations closest to the ice shelf (Group a) produced the least negative $\delta^{18}\text{O}$ values for mCDW. Since the mCDW closest to the ice shelf is the water that will be melting the ice shelf, and samples from both locations fall on the same $\delta^{18}\text{O}$ -salinity mixing line, this is not thought to be a problem for our analysis. In all other years, the greatest variability in mCDW $\delta^{18}\text{O}$ was in 2014, with a total spread of 0.03‰ (st. dev. 0.01‰) — well within $\pm 0.04\text{‰}$ (0.02 ‰) instrument precision for IRMS (CRDS).

As with mCDW, we see little geographical impact on the calculated average meteoric water column inventory. In almost all cases, the small differences in geography are well below the uncertainty of the calculations. The one exception is 2014, where the stations nearest the Thwaites Glacier Tongue (TGT) exhibit significantly higher meteoric water content than the rest of the study area. While this is consistent with known circulation in the area (Jenkins et al., 2010; Thurnherr et al., 2014; Naveira Garabato et al., 2017; Joughin et al., 2021b), we do not have comparable samples from other years, so those stations were excluded for the purposes of interannual comparisons.

A5 On measuring precipitation in surface waters

The size of the meteoric water fraction calculated using the three-endmember mixing model is inversely proportional to the (negative) magnitude of the meteoric water endmember, as a -15‰ endmember will produce ~1.8x the calculated meteoric water fraction of a -29‰ endmember. For a given mixture, it would thus take ~2x as much -15‰ water to produce the $\delta^{18}\text{O}$ signature than for -29‰ water.

A5 The impact of precipitation on meteoric water inventories

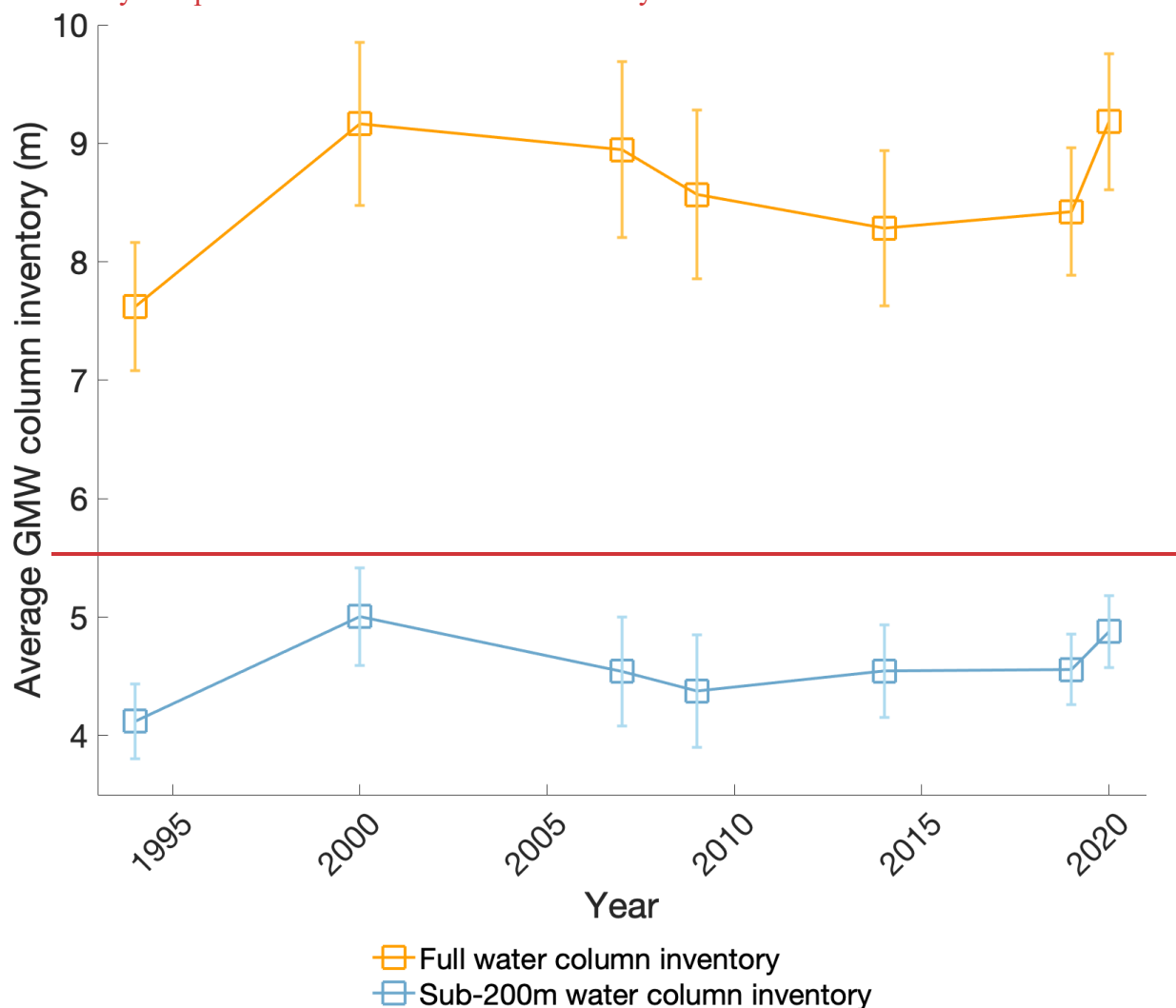
Sea-level precipitation at this latitude has $\delta^{18}\text{O}$ values of ~-15‰ (based on snow collected during NBP19-01, consistent with expected local values from other studies; Gat and Gonfiantini, 1981; Ingraham, 1998; Noone and Simmonds, 2002; Masson-Delmotte et al., 2008). This region of the Amundsen Sea receives ~0.5 m water equivalent of precipitation per year (Donat-Magnin et al., 2021), and mCDW on the shelf has a residence time of ~2 years (Tamsitt et al., 2021). We recalculated water column meteoric water inventories assuming 1 m (2 full years) of local precipitation (-15‰ $\delta^{18}\text{O}$) in the upper 200 m of the water column at the time of sampling.

We find that adding 1 m of precipitation to the water column decreases the amount of meteoric water (as defined using the zero-salinity intercepts,) by an average of 0.55 ± 0.01 m, and decreases sea ice melt by an average of 0.57 ± 0.03 m (Table A4). These results suggest that even with two year's worth of precipitation present in the water column at the time of sampling, the calculated meteoric water inventory could consist of >92% glacial meltwater.

845

Sea-level precipitation at this latitude has $\delta^{18}\text{O}$ values of $\sim -15\text{‰}$ (snow collected at 72°S during NBP19-01). This region of the Amundsen Sea receives $\sim 0.5\text{ m}$ water equivalent of precipitation per year (Donat Magnin et al., 2020). In an extreme case, we could assume that the entirety of 1 year's 0.5 m of precipitation is present in the upper water column at the time of sampling. Given the mathematical relationships above, that would result in a $\sim 0.28\text{ m}$ overestimation of the total glacial meltwater. The lowest (highest) year for average meltwater column inventory 1994, 7.7 m (2020, 9.2 m) corresponds to only a 3.6% (3.0%) overestimation. Even assuming the highest snowfall rates in the region ($\sim 1\text{ m}$ water equivalent near Abbot and Getz Ice Shelves; Donat Magnin et al., 2020) this results in an overestimate of $<8\%$. The largest impact of uncertainty around precipitation is thus lower than uncertainty associated with analytical precision and endmember uncertainty.

850

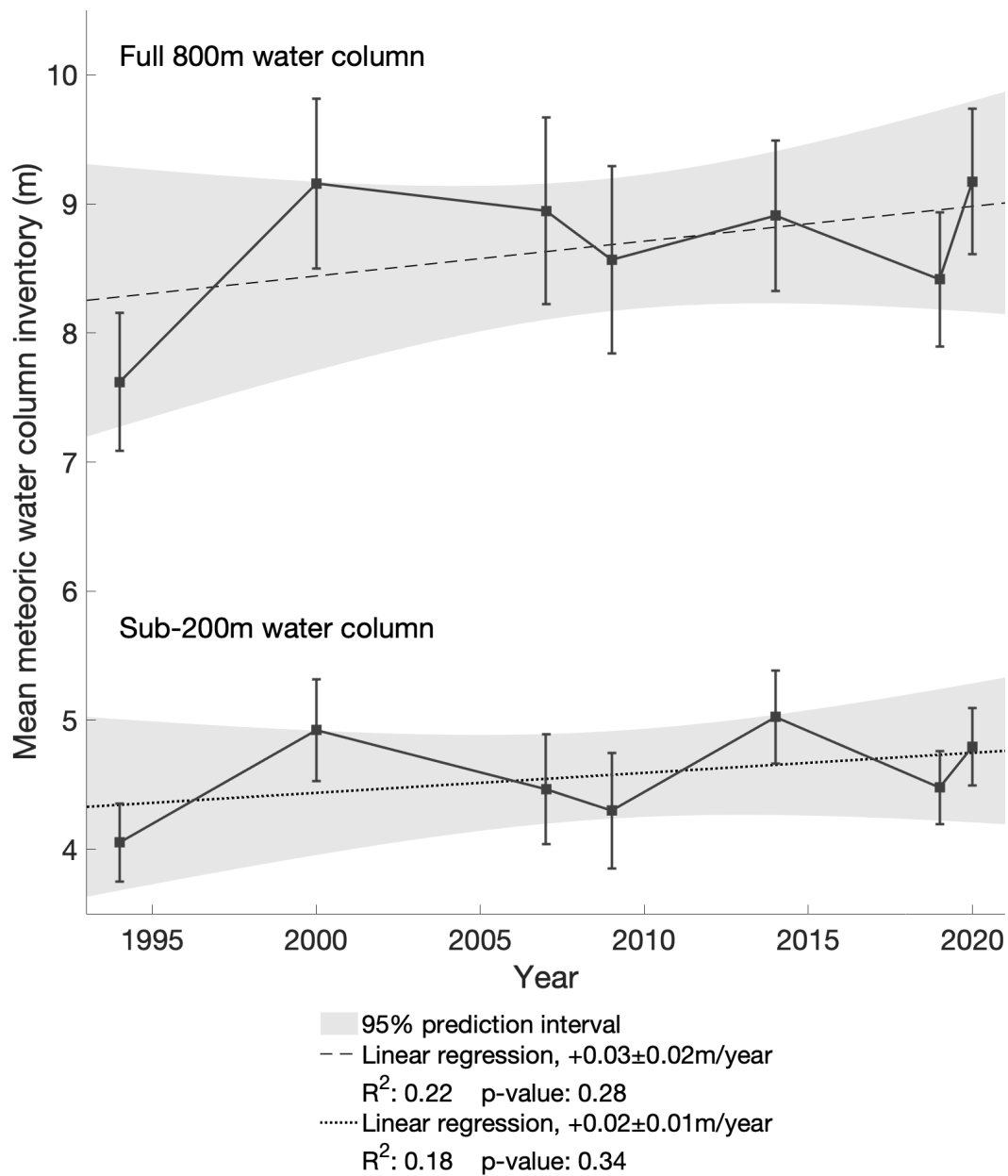


855

Figure A44: Impact of precipitation on total meteoric water Average meltwater column inventory. Mean meteoric water in study area. As Figure 4 from main text, but also showing meltwater inventory is the integrated mean meteoric water content between the surface 200 m and 800 m . The upper water column will include meteoric water from both precipitation, and GMW introduced at depth and mixed upward. The three rightmost columns in the table show the impact on meteoric and sea ice melt water column inventories of

recalculating column inventories (meteoric water $\sim 30\text{‰ } \delta^{18}\text{O}$, Table 2) assuming 2 years of precipitation ($\sim 15\text{‰ } \delta^{18}\text{O}$) in the water column at the time of sampling.

<u>Year</u>	<u>Mean meteoric water inventory (m)</u>	<u>Impact of 1 m (~2 years) precipitation ($-15\text{‰ } \delta^{18}\text{O}$)</u>		
		<u>Change in (glacial) meteoric water (m)</u>	<u>Change in sea ice melt water (m)</u>	<u>Estimated water column glacial meteoric water</u>
<u>1994</u>	<u>7.62</u>	<u>-0.56</u>	<u>-0.61</u>	<u>92.6%</u>
<u>2000</u>	<u>9.16</u>	<u>-0.57</u>	<u>-0.62</u>	<u>93.8%</u>
<u>2007</u>	<u>8.95</u>	<u>-0.56</u>	<u>-0.55</u>	<u>93.7%</u>
<u>2009</u>	<u>8.57</u>	<u>-0.55</u>	<u>-0.55</u>	<u>93.5%</u>
<u>2014</u>	<u>8.93</u>	<u>-0.54</u>	<u>-0.55</u>	<u>94.0%</u>
<u>2019</u>	<u>8.42</u>	<u>-0.54</u>	<u>-0.57</u>	<u>93.6%</u>
<u>2020</u>	<u>9.18</u>	<u>-0.56</u>	<u>-0.54</u>	<u>93.9%</u>



860

Figure A5: Mean meteoric column inventory for each sampled year. Points (blue bars) represent the depth-integrated meltwater volume from the Gaussian Process fit (grey lines in Figure 3) between 200 and 800 m depth. Error bars show the uncertainty in mean meteoric water column inventory associated with analytical precision and environmental variability (Data and Methods 2.2). The relative year-to-year inventories here show the same general empirical trend (within uncertainty) as Figure 4. 2014 shows the highest sub-200m meteoric water content, owed to the sampling immediately alongside TIS - directly in the pathway of glacial meltwater from PIIS (Wählin et al., 2021).

865

Figure A5 and Table A5 show a comparison of the yearly inventories in the total water column vs the water column deeper than 200 m. Both the full and partial water columns show the same relative trend in meteoric water content, indicating that the observed variability is not an effect of interannual variability in precipitation.

Table A5: Relative Fractions of yearly meteoric water inventory in the 800m depth, and 200-800m of full water column. Reported column inventories are the depth integration of the Gaussian fit of all measurements in the field area between the specified depths. The Relative fraction is the normalized relative volume of the average inventory from year to year.

Year	0 m – 800 m		200 m – 800 m		Fraction of total <u>meteoric water</u> in upper 200 m
	Column Inventory, <u>meteoric water</u> (m)	<u>Normalized relative</u> fraction	Column Inventory, <u>meteoric water</u> (m)	<u>Normalized relative</u> fraction	
1994	7.6±0.5	83±6.0±5.9	4.1±0.3	8182.3±6.3	45.9%
2000	9.2±0.7	10099.8±7.5	5.0±0.4	98100±8.2	45.4%
2007	9.0±0.7	97.4±8.1	4.5±0.5	8990.7±9.1	49.2%
2009	8.6±0.7	93±.3±7.8	4.4±0.5	8687.4±9.4	48.9%
2014	8.93±0.67	97±690.2±7.2	5.14.6±0.4	10090.8±7.8	42.745.1%
2019	8.4±0.5	92±691.7±5.8	4.6±0.3	8991.1±6	45.9%
2020	9.2±0.6	100.0±6.3	4.9±0.3	9597.5±6.1	46.9%

875

A6 Sea ice melt and mCDW fractions

A6.1 Sea ice melt

880 While the primary focus of discussion in this paper is meteoric water, the three-endmember mixing model also yields sea ice meltwater fractions. In locations where integrated sea ice melt fractions are negative, net sea ice formation at the time of sampling is indicated. Using a less negative meteoric water $\delta^{18}\text{O}$ endmember (e.g. -25‰ used in Biddle et al., 2019) will result in higher meteoric water fractions and lower sea ice melt fractions, significantly impacting areas/years of net sea ice melt/formation (Figure A7). Since >92% of the meteoric water content in the study area is estimated to be basal melt,
885 using a GMW meteoric water endmember (or close to) will produce more accurate net sea ice melt/formation inventories (and correspondingly more accurate meteoric water inventories).

890 In 2007, 2009, and 2014 positive ice melt fractions >200 m, likely the resulted from samples compromised before analysis. Evaporation leads to positive fractionation of seawater $\delta^{18}\text{O}$, leading to a less-depleted $\delta^{18}\text{O}$ observation at time of analysis; less depleted $\delta^{18}\text{O}$ relative to salinities fresher than mCDW will be interpreted by the 3-endmember mixing model as sea ice melt. The stratification in this region makes it unlikely that there are significant sea ice melt fractions below 200 m. As with the $\delta^{18}\text{O}$ -salinity () and meteoric water-depth (Figure 3) plots, 1994, 2000, 2019 and 2020 exhibit the tightest distribution, suggesting higher quality data. Grey lines show the Gaussian process fit, and points are shaded to show sample $\delta^{18}\text{O}$.
895

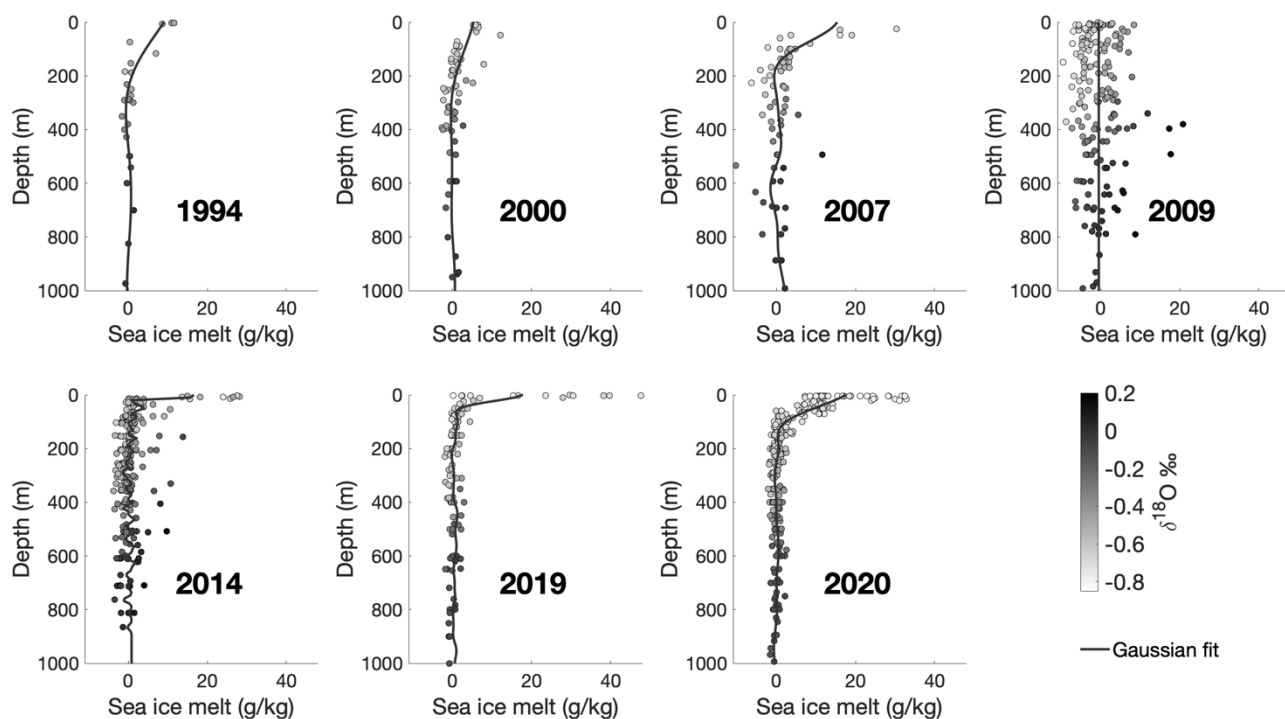


Figure A6: Sea ice melt fractions vs depth. Calculated sea ice melt fractions using salinity and $\delta^{18}\text{O}$ measurements in 3-endmember mixing model. Shading of dots indicates the measured $\delta^{18}\text{O}$ of that sample. In several years (2014-2020) there is a high concentration of sea ice melt near the surface, and very little extending deeper than 200 m. Negative values indicate net sea ice formation. Years with greater sea ice melt (2007, 2020) than sea ice formation show greater divergence from the mCDW-GMW mixing line in surface waters ().

Table A6: Sea ice melt column inventories and uncertainty. Mean sea ice melt column inventories are produced by depth integrating the Gaussian process fit (grey lines **Figure A6**) between the surface and 800m. Uncertainty as described in **Appendix A3**.

<u>Year</u>	<u>Mean sea ice melt column inventory (m)</u>	<u>Sea ice melt fraction uncertainty (g/kg)</u>
<u>1994</u>	<u>1.0\pm0.8</u>	<u>1.9</u>
<u>2000</u>	<u>0.6\pm0.9</u>	<u>2.1</u>
<u>2007</u>	<u>1.2\pm0.9</u>	<u>2.2</u>
<u>2009</u>	<u>-0.4\pm1.0</u>	<u>2.2</u>
<u>2014</u>	<u>0.5\pm0.9</u>	<u>2.0</u>
<u>2019</u>	<u>1.0\pm0.7</u>	<u>1.4</u>
<u>2020</u>	<u>1.1\pm0.8</u>	<u>1.7</u>

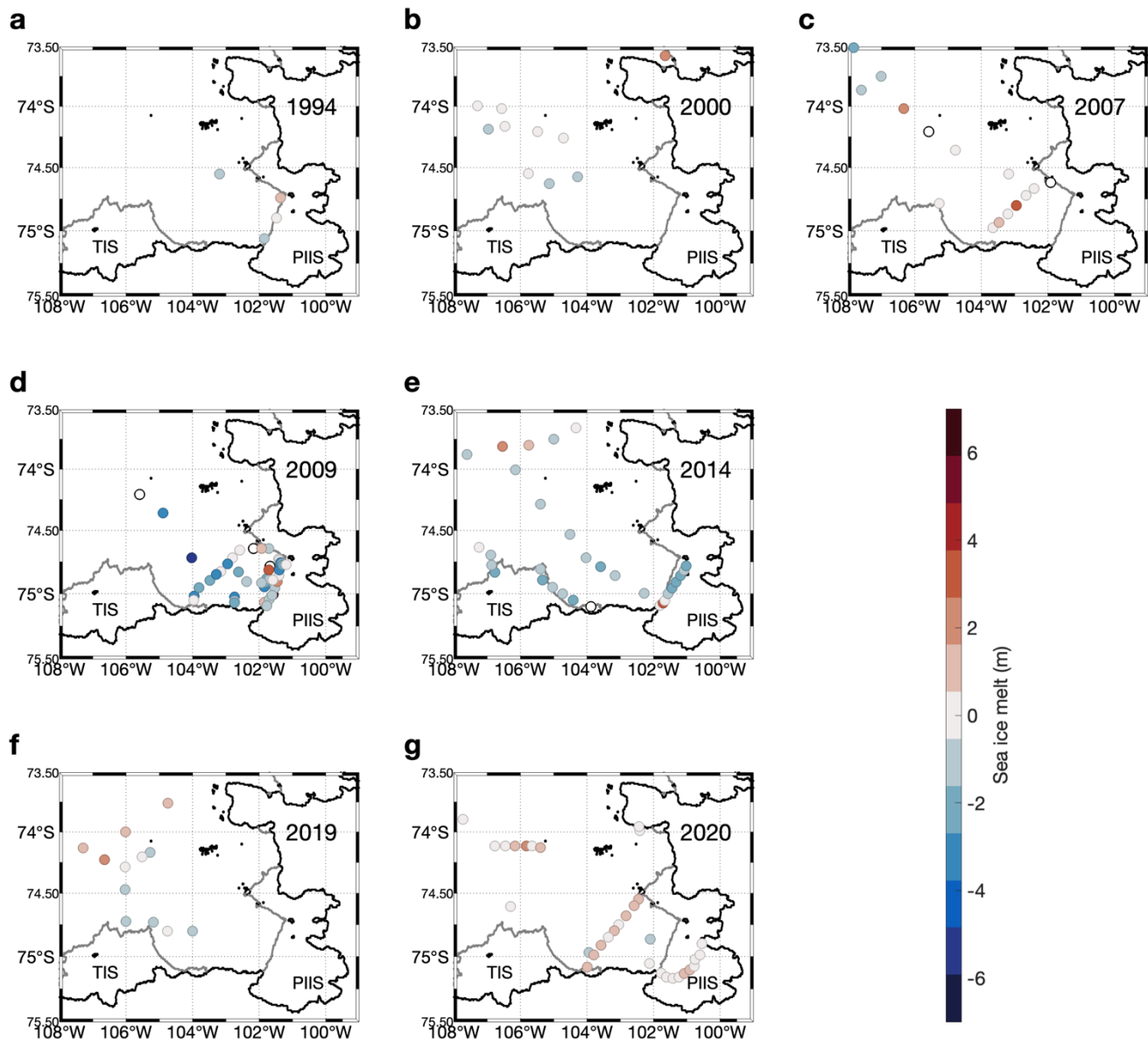


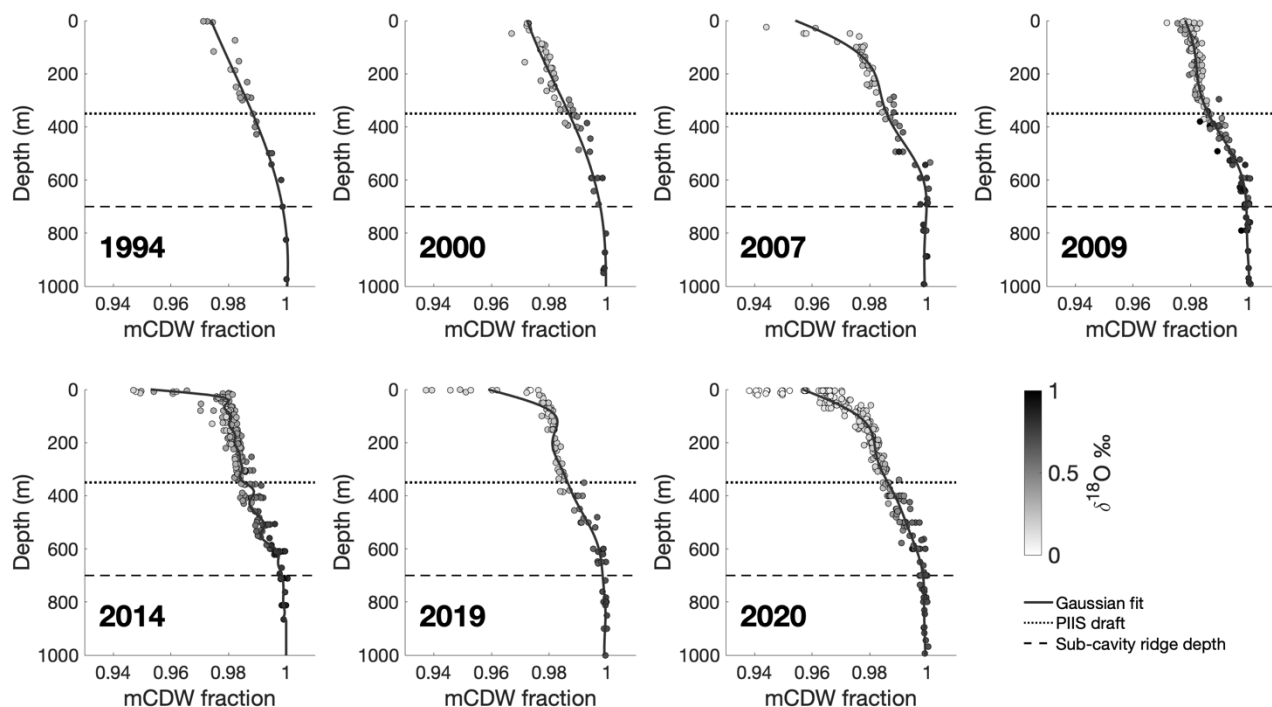
Figure A7: Integrated sea ice melt fractions at sampling locations each year. Negative sea ice melt fractions indicate areas of net sea ice formation. Stations with partial water column sampling show only partial inventories. White dots with black outlines are stations where only one depth was sampled (2007, 2009, 2014). Years with greater sea ice melt (2007, 2020) than formation show greater divergence from the mCDW-GMW mixing line in surface waters ().

905

910

A6.2 mCDW fractions

Waters deeper than ~800m are comprised of pure mCDW; moving toward the surface, meteoric freshwater from basal melt is introduced starting at ~700m. The near surface waters are rich in meteoric water and/or sea ice melt are comprised of >92% mCDW (Figure A8).



915 **Figure A8: mCDW fractions vs depth.** Calculated mCDW fractions using salinity and $\delta^{18}\text{O}$ measurements in 3-endmember mixing model. Shading of dots indicates the measured $\delta^{18}\text{O}$ of that sample. Deep waters (>800m) characterize relatively unadulterated mCDW, while near surface waters contain the highest concentrations of sea ice melt and meteoric water. Dotted horizontal lines show the depth of the PIIS draft, and dashed lines show the depth of the PIIS sub-cavity ridge.

920 **Table A7: mCDW column inventories and uncertainty.** Mean sea ice melt column inventories are produced by depth integrating the Gaussian process fit (grey lines **Figure A8**) between the surface and 800m. Uncertainty as described in **Appendix A3**.

<u>Year</u>	<u>Mean mCDW column inventory (m)</u>	<u>mCDW fraction uncertainty (g/kg)</u>
<u>1994</u>	<u>781.2±0.3</u>	<u>0.6</u>
<u>2000</u>	<u>780.1±0.4</u>	<u>0.6</u>
<u>2007</u>	<u>779.8±0.3</u>	<u>0.7</u>
<u>2009</u>	<u>781.6±0.2</u>	<u>0.6</u>
<u>2014</u>	<u>780.4±0.5</u>	<u>0.7</u>
<u>2019</u>	<u>780.6±0.2</u>	<u>0.5</u>
<u>2020</u>	<u>779.6±0.5</u>	<u>0.8</u>

A6A7 2009 Sample quality control

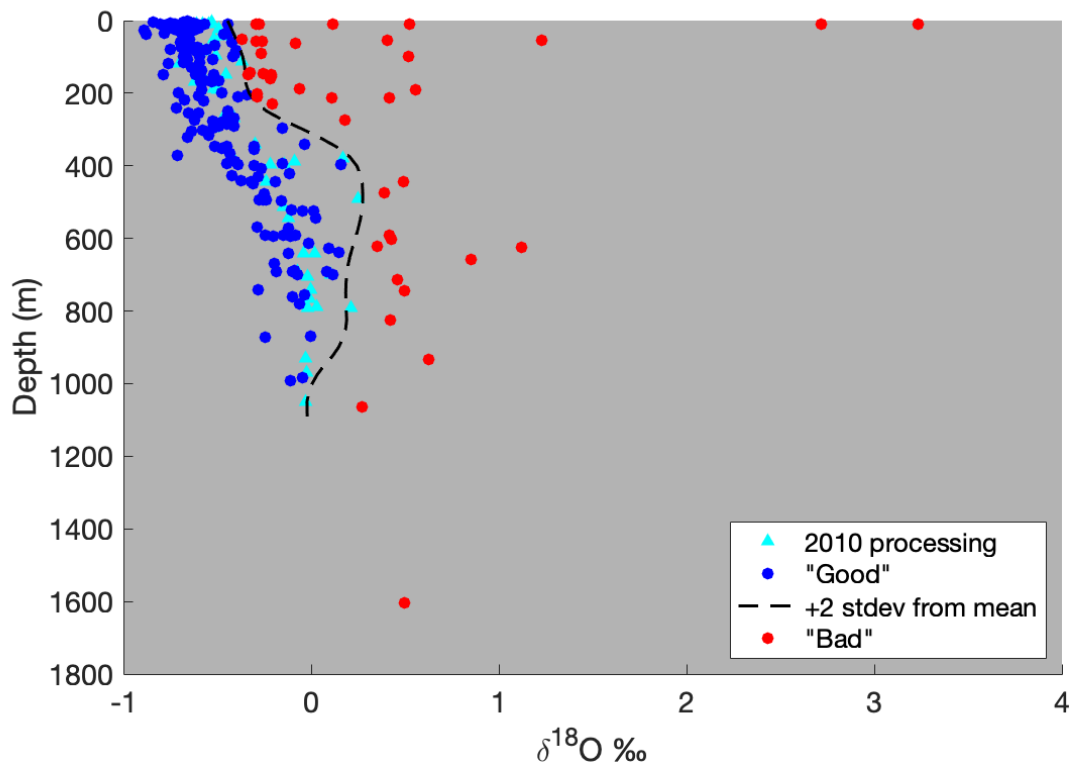
925 A ~~subset~~ portion of the samples for 2009 were analyzed on an IRMS in 2010, while the ~~remainder~~ rest were stored until a 2020 CRDS analysis. At the latter time, 56% of the samples analyzed contained an unknown, clear, needle-shaped precipitate. Several bottles also had a lower-~~than-~~expected sample volume, suggesting evaporation, which would ~~likely have altered the~~ be expected to alter $\delta^{18}\text{O}$ content ~~via~~ through isotopic fractionation. Several steps were taken to ensure the quality of samples analyzed after a decade in storage.

930 **A6.1A7.1 SEM EDS Analysis of Precipitate**

Samples of the precipitate were extracted from multiple sample bottles and analyzed using a Scanning Electron Microscope, equipped with a FEI Magellan 400 XHR SEM with Bruker Quantax XFlash 6 | 60 SDD EDS detector, at the Stanford Nano Shared Facilities (SNSF). Peaks were observed at the spectra associated with Mg, Si, and O, indicating the precipitate is likely some form of Magnesium Silicate Hydroxide ($\text{Mg}_3\text{Si}_2\text{O}_5(\text{OH})_4$), or Magnesium Silicate Hydrate ($\text{Mg}_2\text{Si}_3\text{O}_8 \cdot \text{H}_2\text{O}$). $\text{Si}(\text{OH})_4$ is the simplest soluble form of silica and is found universally in seawater at low concentrations (Belton et al., 2012). 935 The maximum amount of silicate that could be expected in this area of the ocean is $\sim 100 \mu\text{mol/kg}$ (Rubin et al., 1998). In this case, even if the entire $100 \mu\text{mol/kg}$ of Si were drawn down to 0, solely into a Magnesium Silicate, with a very high fractionation factor, e.g. the -40‰ reported for diatoms (Leclerc and Labeyrie, 1987) the greatest effect on a sample would be 0.0003‰ – well below the analytical 940 precision of the CRDS (0.025‰) or IRMS (0.04‰). Therefore, it is highly unlikely that the precipitate contributed a detectable fractionation or alteration of seawater $\delta^{18}\text{O}$ in our samples.

A6.2A7.2 Quality control for evaporation

945 In all years, the bulk of ~~Assuming accurate 2020 analyses,~~ the $\delta^{18}\text{O}$ data fall in a broadly predictable pattern, less depleted at depths below $\sim 600\text{m}$, and more depleted near the surface. Values >2 standard deviations from this pattern denote samples that ~~were likely subject to~~ experienced significant evaporation (Figure A9 ~~Figure A9~~)



950 **Figure A9: $\delta^{18}\text{O}$ vs depth for all 2009 samples, coded for likelihood of evaporation.** The dashed line represents +2 standard deviations from a moving depth-averaged $\delta^{18}\text{O}$ based on the 2010 [processing data](#), beyond which the results are unacceptable. Archivable data will be made available upon publication.

955 As a secondary check, the $\delta^{18}\text{O}$ of all samples was plotted vs depth with a qualitative indicator of the amount of precipitate found in the sample vial ([Figure A10](#)[Figure A10](#)) to see if any patterns emerged compared to that of depth-comparable samples [processed](#) in 2010. No clear trend was evident.

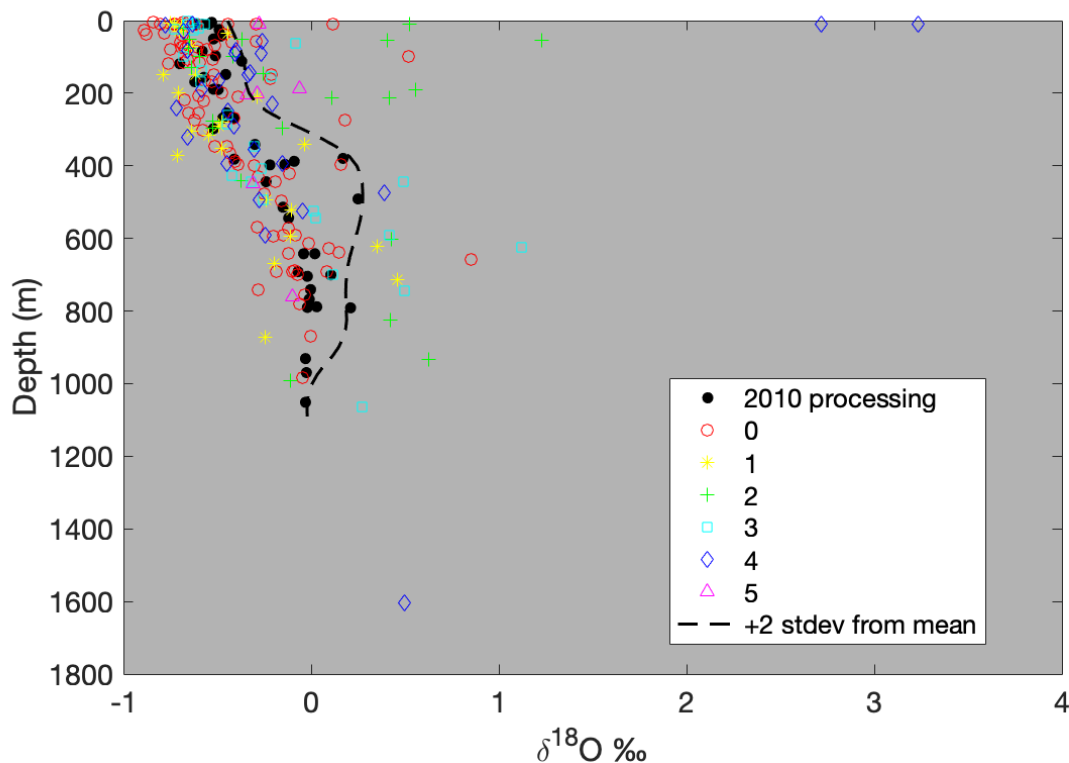


Figure A10: $\delta^{18}\text{O}$ vs depth of all 2009 samples, coded by amount of precipitate present. Each bottle was graded by eye based on the volume of precipitate present with 0 being no precipitate present, and 5 being the most precipitate present. As with Figure A9, Figure S3, the ~~dashed~~ line represents +2 standard deviations from the mean $\delta^{18}\text{O}$ at each depth.

960

Evaporation is accompanied by isotopic fractionation, with H_2^{16}O ~~evaporating~~ evaporates preferentially, leaving the remaining liquid relatively enriched in the H_2^{18}O . Evaporation also increases the salinity and thus density of the remaining sample, ~~thereby increasing sample density~~. We measured the density of each seawater sample 5 times using a calibrated 1ml pipet and mg balance. The theoretical density of each sample was calculated from its associated CTD salinity and temperature, ~~during weight determination~~. Differences between measured and theoretical densities for each sample are plotted in Figure A11 Figure A11.

965

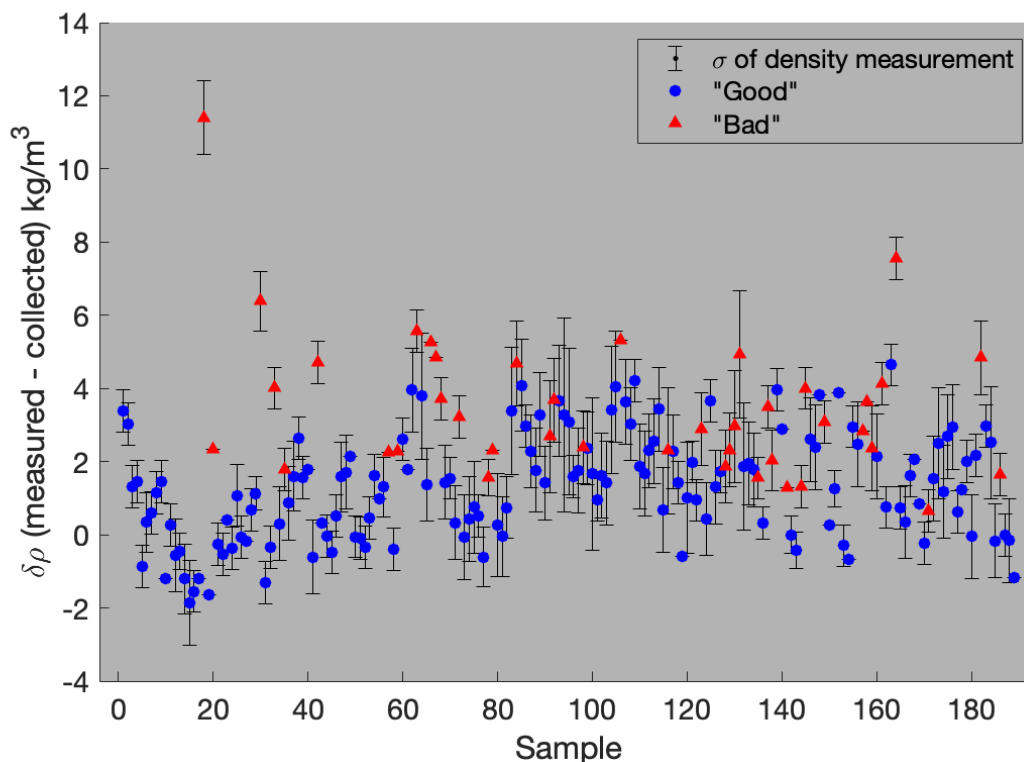


Figure A11: Difference in measured density vs theoretical density for each 2009 sample analyzed in 2020. Theoretical density is based on CTD salinity at each sample location, and measured density calculated from 1ml sample aliquots weighed on a mg scale, with sample coding as in [Figure A9](#), [Figure A5](#). Error bars represent the standard deviation of replicates for each measurement.

While a few samples show clear evidence of evaporation, and correspondingly high $\delta^{18}\text{O}$ values, most show less obvious density anomalies, exposing the limitations of our scale accuracy at that level. 75% of the samples measured showed a higher than expected density and 25% the remainder measured a lower than expected density. [Figure A11](#) [Figure A7](#) displays a significant overlap in measured density space between samples previously identified as “good” or “bad” ([Figure A9](#) [Figure A5](#)). [Figure A11](#) [Figure A7](#) shows that there are no samples flagged as compromised (“bad”) from our earlier depth-based analysis (“bad”) with a $\delta\rho$ greater than 1.3 kg/m³. At an aggressive first pass, we removed all sample data with a $\delta\rho$ greater than 1.3 kg/m³ and looked at each hydrocast profile individually, using the remaining data. ~~Excluded~~ We then added those excluded samples flagged as “good” ~~were returned to back into~~ the dataset, and [individual profiles](#) re-scrutinized individual profiles to check for any qualitative [anomalies](#) change.

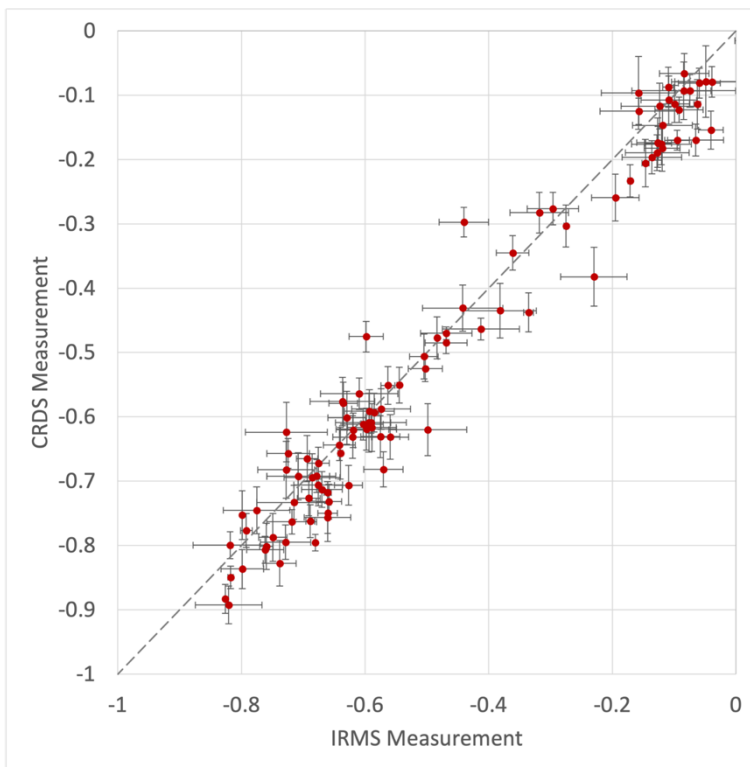
[A6.3](#) [A7.3](#) Conclusion and final 2009 sample inclusion

While it is ~~very extremely~~ unlikely that the precipitate ~~changed~~ contributed to a change in sample values, some samples do appear to have been subject to evaporation. The inclusion of all samples flagged as

“Good” does not qualitatively change ~~our~~the analyses ~~presented in this study~~when compared with ~~the analyses using only these~~ data ~~processed~~run in 2010. We exclude ~~the~~ 41 samples initially flagged as “Bad,” (~~Figure A9~~~~Figure A5~~) and retain the remaining 148 flagged as “Good”.

990 **A7A8 CRDS and IRMS cross-calibration**

We ~~processed~~ran 100 samples from 2019 and 2020 concurrently using the Picarro L2140-i CRDS, ~~and~~ on a Finnigan MAT252 IRMS (~~Figure A12~~Figure A12) using CO₂ equilibration (Epstein and Mayeda, 1953). Both instruments were independently calibrated using international standards VSMOW, SLAP, and GISP, and all samples were run in duplicate. The data from both machines was comparable, with the Picarro achieving a precision of 0.02‰, ~~‰ on replicates,~~ and the IRMS achieving a precision of 0.03‰ on replicates. ~~The~~ ~~On average the~~ offset between ~~the~~ CRDS ~~data~~ and IRMS data ~~averaged~~was -0.02‰, with the CRDS data being more negative, ~~than that from the IRMS.~~ Since the offset between the two machines was less than either instrument's precision, data from the CRDS was used as-is. ~~Values~~The values reported for the CRDS are the average of 6 individual injections/measurements from each vial; ~~reported~~precision is ~~reported~~ based on the standard deviation between multiple 6-injection averages from replicate analyses, separated by days, weeks, or months.



005 **Figure A12: 101 seawater δ¹⁸O samples collected in 2019 and 2020 analyzed with both CRDS and IRMS.** Each point represents the value obtained by measuring the same sample on the IRMS (x-axis) and the CRDS (y-axis). ~~Error~~Horizontal error bars represent the ~~corresponding~~ standard deviation of the IRMS ~~and~~ CRDS measurements, ~~and~~ vertical error bars represent the standard deviation of the ~~CRDS measurement.~~

A8A9 CRDS Methods

010 570A large number of the isotope samples for this study (all samples from 2019 and 2020, portions from 2007 and 2009) were run on a Picarro L2140-i CRDS system, rather than a traditional IRMS. Using this system, we were able to achieve an average precision of <0.02‰ on multiple replicate analyses.

015 Samples were collected in 10ml or 30ml glass serum vials (Fisher Scientific part number: 06-406D/06-406F), sealed with rubber stoppers (Fisher Scientific part number: 06-406-11B) and aluminum seals (Fisher Scientific part number: 06-406-15).

020 Sample vials should be filled to just below the “neck” (narrowest part). Minimizing the headspace of the vial is important for minimizing evaporation, however it is important to leave *some* headspace to allow for expansion/contraction of the sample (if collecting samples larger than 30 ml, slightly more headspace should be left, with 250 ml vials being filled to ~1/2 way up the “shoulder” before the neck). When sealing serum vials with rubber stoppers and aluminum seals, it is important that the tops of the aluminum seals are crimped tightly but remain flat after crimping/capping. An upward “buckling” of the aluminum seal indicates over-crimping and will produce an inferior seal.

025 Internal lab (Stanford SIL) data shows that samples can be preserved in this manner for up to 5 years without significant degradation, while bottles with threaded caps and parafilm reliably maintain sample integrity below instrumental precision for no more than 1 year.

030 -The instrument setup used was as follows:

- 10µl syringe (Trajan Part number: 002982)
- A single standard or unknown run consists of 7 injections (measurements) per sample
- Sample injection volume 2.2 µl
- 035 • 3x 5µl rinses with fresh water from inkwell (IW) between each sample
- 3x 2.2µl rinses with sample before first measurement of new sample or standard vial
- Rinse only between sample vials, or 1 rinse for every 7 standard or unknown injections.

Several~~In addition to the above instrument method, several~~ protocols were also followed with regards to sample and instrument handling.

- 040 • Fresh vial of internal lab standard (ILS) used each day. The ILS was prepared to have a $\delta^{18}\text{O}$ in the middle of the range expected from the unknowns (i.e. \sim -0.3‰) to minimize memory issues between samples. The IW was also filled with water of approximately this composition.
- A fresh 2ml vial of ILS was used each day, and discarded at the end of the sequence.

- 045
- Samples were pipetted from sealed 10ml or 30ml serum into 2ml vials ([Fisher Scientific part number: 03-391-15](#)) for analysis on the day they were to be analyzed. The 2ml vials used for analysis were found to only reliably preserve sample $\delta^{18}\text{O}$ for <1 week.
 - After each sequence, the syringe was cleaned with DI water, and then rinsed thoroughly with water from the Inkwell, to minimize memory/contamination issues of residual water left in the syringe.
 - Treated in this way, syringes can be expected to last [for](#) 1500 to 2500 injections
 - Fresh vaporizer septa ([Trajan Partpart number: 0418240](#)) was used every day
 - ILS were analyzed no less than every 5th unknown, and no fewer than 3 ILS were measured per run
 - [An ILS](#)
- 050
- 055
- All data were corrected based on the slope of the ILS measurements over the course of the sequence.
 - Each run began with no fewer than 10 injections from the IW, to allow the instrument to reach baseline.
 - Syringe cleaned thoroughly with DI water each day, and manually rinsed with IW water prior to sequence.
 - No more than 5 unknowns (7 injections each) measured between run of ILS (7 injections)
 - ILS measured at least 3 times during each sequence – at the beginning, end, and midpoint. least 3 standards measured during each sequence.
- 060

A typical 24h sequence ran 16 unknowns. The sequence was set up, as follows:

- 065
- 15 injections from IW
 - ILS (7 injections)
 - 4 unknowns (4x7 injections)
 - ILS (7 injections)
 - 4 unknowns (4x7 injections)
- 070
- ILS (7 injections)
 - 4 unknowns (4x7 injections)
 - ILS (7 injections)
 - 4 unknowns (4x7 injections)
 - ILS (7 injections)

075 Overall, this sequence consists of 162 injections, 112 of which contained salt, for a vaporizer load of
| ~8.6 mg of salt/day.

The instrument vaporizer was cleaned at least every 200mg worth of salt injected.

- @ 35PSU & 2.2 μ l injections, this is 2597 salty injections, or 371 samples @ 7 injections each.
(~ every 23 analytical days)

080 Finally, analytical data quality control was conducted in the following way

- The first injection of each sample was discarded, to minimize instrument memory issues
- If the standard deviation of the remaining 6 injections was >0.04‰, up to one outlier could be removed. Any samples where the standard deviation of measured values was still >0.04‰ were rerun the following day from the same vial, using the same septa.
- 085 • If a rerun would not be possible the following day, the vial septa was replaced with a new one.
- Data from each hydrocast were inspected as a group. Any samples that appeared inconsistent with the rest of the hydrocast (e.g. with regards to salinity, or neighboring $\delta^{18}\text{O}$ values) were rerun. If the rerun occurred within 1 week of the initial run, the same vial was used. Otherwise, a fresh aliquot of sample was drawn from the resealed serum vial.

090 **Data availability**

| All data, excluding that flagged as “bad,” (Appendix A7) used in this study can be accessed at:
<https://doi.org/10.25740/zf704jg7109>

Author contributions:

Conceptualization: RBD

095 Methodology: RBD, ANH, DAM

Investigation: ANH, DAM, RBD

Visualization: ANH

Funding acquisition: RBD

Project administration: RBD

100 Supervision: RBD

Writing – original draft: ANH

Writing – review & editing: ANH, SSJ, RBD, DAM, RAM

Contribution of data: ANH, DAM, RBD, SSJ, RAM

105 **Competing interests**

The authors declare that they have no conflict of interest.

Acknowledgments

110 We acknowledge the staff and crew of ~~Nathaniel B. Palmer~~~~NBP~~ cruises 94-02, 00-01, 07-02, 09-01, 19-01, 20-02, and iSTAR2014 for ~~assistance with support of the~~ data acquisition. We extend special thanks to Isa Rosso, Michael ~~Burnett~~~~Burnette~~, and Emilia Fercovic for their help with sample collection. ~~We thank~~ MAC3 Impact Philanthropies ~~assisted~~~~for assistanee~~ with CRDS instrumentation and development. Peter Schlosser & Ronny Friedrich ~~provided~~~~for~~ the 2007 CRDS data, and Shigeru Aoki ~~was consulted regarding~~~~for his consultation on~~ the 2014 data offset. Thanks also to Cindy Ross and Stanford Nano Shared Facilities, supported by NSF ECCS-2026822 for SEM analyses.

115

Funding: This project was funded by NSF:

NSF-OPP-1644118

NSF-OPP-1644159

References

- 120 Adusumilli, S., Fricker, H. A., Medley, B., Padman, L., and Siegfried, M. R.: Interannual variations in meltwater input to the Southern Ocean from Antarctic ice shelves, *Nat. Geosci.*, 13, 616–620, <https://doi.org/10.1038/s41561-020-0616-z>, 2020.
- Assmann, K. M., Hellmer, H. H., and Jacobs, S. S.: Amundsen Sea ice production and transport, *J. Geophys. Res. Oceans*, 110, <https://doi.org/10.1029/2004JC002797>, 2005.
- 125 Belton, D. J., Deschaume, O., and Perry, C. C.: An overview of the fundamentals of the chemistry of silica with relevance to biosilicification and technological advances, *Febs J.*, 279, 1710–1720, <https://doi.org/10.1111/j.1742-4658.2012.08531.x>, 2012.
- Benetti, M., Sveinbjörnsdóttir, A. E., Ólafsdóttir, R., Leng, M. J., Arrowsmith, C., Debondt, K., Fripiat, F., and Aloisi, G.: Inter-comparison of salt effect correction for $\delta^{18}\text{O}$ and $\delta^2\text{H}$ measurements in seawater by CRDS and IRMS using the gas-H₂O equilibration method, *Mar. Chem.*, 194, 114–123, <https://doi.org/10.1016/j.marchem.2017.05.010>, 2017.
- 130 Biddle, L. C., Heywood, K. J., Kaiser, J., and Jenkins, A.: Glacial Meltwater Identification in the Amundsen Sea, *J. Phys. Oceanogr.*, 47, 933–954, <https://doi.org/10.1175/JPO-D-16-0221.1>, 2017.
- Biddle, L. C., Loose, B., and Heywood, K. J.: Upper Ocean Distribution of Glacial Meltwater in the Amundsen Sea, Antarctica, *J. Geophys. Res. Oceans*, 124, <https://doi.org/10.1029/2019JC015133>, 2019.
- 135 Blunier, T. and Brook, E. J.: Timing of Millennial-Scale Climate Change in Antarctica and Greenland During the Last Glacial Period, *Science*, 291, 109–112, <https://doi.org/10.1126/science.291.5501.109>, 2001.

- Christie, F. D. W., Steig, E. J., Gourmelen, N., Tett, S. F. B., and Bingham, R. G.: Inter-decadal climate variability induces differential ice response along Pacific-facing West Antarctica, *Nat. Commun.*, 14, 93, <https://doi.org/10.1038/s41467-022-35471-3>, 2023.
- 140 Coplen, T. B.: Reporting of stable hydrogen, carbon, and oxygen isotopic abundances (Technical Report), *Pure Appl. Chem.*, 66, 273–276, <https://doi.org/10.1351/pac199466020273>, 1994.
- Dierssen, H. M., Smith, R. C., and Vernet, M.: Glacial meltwater dynamics in coastal waters west of the Antarctic peninsula, *Proc. Natl. Acad. Sci.*, 99, 1790–1795, <https://doi.org/10.1073/pnas.032206999>, 2002.
- 145 Donat-Magnin, M., Jourdain, N. C., Kittel, C., Agosta, C., Amory, C., Gallée, H., Krinner, G., and Chekki, M.: Future ice-sheet surface mass balance and melting in the Amundsen region, West Antarctica, *The Cryosphere*, <https://doi.org/10.5194/tc-2020-113>, 2020.
- Donat-Magnin, M., Jourdain, N. C., Kittel, C., Agosta, C., Amory, C., Gallée, H., Krinner, G., and Chekki, M.: Future surface mass balance and surface melt in the Amundsen sector of the West Antarctic Ice Sheet, *The Cryosphere*, 15, 571–593, <https://doi.org/10.5194/tc-15-571-2021>, 2021.
- 150 Dotto, T. S., Naveira Garabato, A. C., Bacon, S., Holland, P. R., Kimura, S., Firing, Y. L., Tsamados, M., Wählin, A. K., and Jenkins, A.: Wind-Driven Processes Controlling Oceanic Heat Delivery to the Amundsen Sea, Antarctica, *J. Phys. Oceanogr.*, 49, 2829–2849, <https://doi.org/10.1175/JPO-D-19-0064.1>, 2019.
- Dotto, T. S., Naveira Garabato, A. C. N., Wählin, A. K., Bacon, S., Holland, P. R., Kimura, S., Tsamados, M., Herraiz-Borreguero, L., Kalén, O., and Jenkins, A.: Control of the Oceanic Heat Content of the Getz-Dotson Trough, Antarctica, by the Amundsen Sea Low, *J. Geophys. Res. Oceans*, 125, e2020JC016113, <https://doi.org/10.1029/2020JC016113>, 2020.
- 155 Dutrieux, P., De Rydt, J., Jenkins, A., Holland, P. R., Ha, H. K., Lee, S. H., Steig, E. J., Ding, Q., Abrahamsen, E. P., and Schroder, M.: Strong Sensitivity of Pine Island Ice-Shelf Melting to Climatic Variability, *Science*, 343, 174–178, <https://doi.org/10.1126/science.1244341>, 2014.
- Epstein, S. and Mayeda, T.: Variation of ^{18}O content of waters from natural sources, *Geochem. Cosmochim. Acta*, 4, 213–224, 1953.
- 160 Flexas, M. M., Thompson, A., Schodlok, M., Zhang, H., and Speer, K.: Antarctic Peninsula warming triggers enhanced basal melt rates throughout West Antarctica, *Sci. Adv.*, 12, 2022.
- Fogwill, C. J., Phipps, S. J., Turney, C. S. M., and Golledge, N. R.: Sensitivity of the Southern Ocean to enhanced regional Antarctic ice sheet meltwater input, *Earths Future*, 3, 317–329, <https://doi.org/10.1002/2015EF000306>, 2015.
- 165 Fretwell, P., Pritchard, H. D., Vaughan, D. G., Bamber, J. L., Barrant, N. E., Bell, R., Bianchi, C., Bingham, R. G., Blankenship, D. D., Casassa, G., Catania, G., Callens, D., Conway, H., Cook, A. J., Corr, H. F. J., Damaske, D., Damm, V., Ferraccioli, F., Forsberg, R., Fujita, S., Gim, Y., Gogineni, P., Griggs, J. A., Hindmarsh, R. C. A., Holmlund, P., Holt, J. W., Jacobel, R. W., Jenkins, A., Jokat, W., Jordan, T., King, E. C., Kohler, J., Krabill, W., Riger-Kusk, M., Langley, K. A., Leitchenkov, G., Leuschen, C., Luyendyk, B. P., Matsuoka, K., Mouginot, J., Nitsche, F. O., Nogi, Y., Nost, O. A., Popov, S. V., Rignot, E., Rippin, D. M., Rivera, A., Roberts, J., Ross, N., Siegert, M. J., Smith, A. M., Steinhage, D., Studinger, M., 170 Sun, B., Tinto, B. K., Welch, B. C., Wilson, D., Young, D. A., Xiangbin, C., and Zirizzotti, A.: Bedmap2: improved ice bed, surface and thickness datasets for Antarctica, *The Cryosphere*, 7, 375–393, <https://doi.org/10.5194/tc-7-375-2013>, 2013.

- Hellmer, H. H., Jacobs, S. S., and Jenkins, A.: Oceanic Erosion of a Floating Antarctic Glacier in the Amundsen Sea, in: *Ocean, Ice, and Atmosphere: Interactions at the Antarctic Continental Margin*, vol. 75, edited by: Jacobs, S. S. and Weiss, R. F., American Geophysical Union, Washington, D. C., 83–99, <https://doi.org/10.1029/AR075p0083>, 1998.
- 175 Heywood, K. J., Biddle, L., Boehme, L., Dutrieux, P., Fedak, M., Jenkins, A., Jones, R., Kaiser, J., Mallett, H., Naveira Garabato, A., Renfrew, I., Stevens, D., and Webber, B.: Between the Devil and the Deep Blue Sea: The Role of the Amundsen Sea Continental Shelf in Exchanges Between Ocean and Ice Shelves, *Oceanography*, 29, 118–129, <https://doi.org/10.5670/oceanog.2016.104>, 2016.
- 180 Holland, P. R., Bracegirdle, T. J., Dutrieux, P., Jenkins, A., and Steig, E. J.: West Antarctic ice loss influenced by internal climate variability and anthropogenic forcing, *Nat. Geosci.*, 12, 718–724, <https://doi.org/10.1038/s41561-019-0420-9>, 2019.
- IPCC: *The Ocean and Cryosphere in a Changing Climate: Special Report of the Intergovernmental Panel on Climate Change*, 1st ed., Cambridge University Press, <https://doi.org/10.1017/9781009157964>, 2022.
- 185 Jacobs, S. S., Fairbanks, R. G., and Horibe, Y.: Origin and evolution of water masses near the Antarctic continental margin: Evidence from H₂ 18O / H₂ 16O ratios in seawater, *Oceanol. Antarct. Cont. Shelf*, 43, 59–85, <https://doi.org/10.1029/AR043>, 1985.
- Jacobs, S. S., Hellmer, H. H., and Jenkins, A.: Antarctic Ice Sheet melting in the southeast Pacific, *Geophys. Res. Lett.*, 23, 957–960, <https://doi.org/10.1029/96GL00723>, 1996.
- Jacobs, S. S., Giulivi, C. F., and Mele, P. A.: Freshening of the Ross Sea during the late 20th century., *Science*, 297, 386–389, <https://doi.org/10.1126/science.1069574>, 2002.
- 190 Jacobs, S. S., Giulivi, C. F., and Dutrieux, P.: Persistent Ross Sea Freshening from Imbalance West Antarctic Ice Shelf Melting, *J. Geophys. Res. Oceans*, n/a, e2021JC017808, <https://doi.org/10.1029/2021JC017808>, 2022.
- Jenkins, A., Dutrieux, P., Jacobs, S. S., McPhail, S. D., Perrett, J. R., Webb, A. T., and White, D.: Observations beneath Pine Island Glacier in West Antarctica and implications for its retreat, *Nat. Geosci.*, 3, 468–472, <https://doi.org/10.1038/ngeo890>, 2010.
- 195 Jenkins, A., Shoosmith, D., Dutrieux, P., Jacobs, S. S., Kim, T. W., Lee, S. H., Ha, H. K., and Stammerjohn, S.: West Antarctic Ice Sheet retreat in the Amundsen Sea driven by decadal oceanic variability, *Nat. Geosci.*, 11, 733–738, <https://doi.org/10.1038/s41561-018-0207-4>, 2018.
- 200 Jeon, M. H., Jung, J., Park, M. O., Aoki, S., Kim, T.-W., and Kim, S.-K.: Tracing Circumpolar Deep Water and glacial meltwater using humic-like fluorescent dissolved organic matter in the Amundsen Sea, *Antarctica, Mar. Chem.*, 235, 104008, <https://doi.org/10.1016/j.marchem.2021.104008>, 2021.
- Joughin, I., Shapero, D., Smith, B., Dutrieux, P., and Barham, M.: Ice-shelf retreat drives recent Pine Island Glacier speedup, *Sci. Adv.*, 7, eabg3080, <https://doi.org/10.1126/sciadv.abg3080>, 2021a.
- Joughin, I., Shapero, D., Dutrieux, P., and Smith, B.: Ocean-induced melt volume directly paces ice loss from Pine Island Glacier, *Sci. Adv.*, 7, eabi5738, <https://doi.org/10.1126/sciadv.abi5738>, 2021b.
- 205 Kim, T.-W., Yang, H. W., Dutrieux, P., Wählin, A. K., Jenkins, A., Kim, Y. G., Ha, H. K., Kim, C.-S., Cho, K.-H., Park, T., Park, J., Lee, S., and Cho, Y. K.: Interannual Variation of Modified Circumpolar Deep Water in the Dotson-Getz Trough, West Antarctica, *J. Geophys. Res. Oceans*, n/a, e2021JC017491, <https://doi.org/10.1029/2021JC017491>, 2021.

- 210 Kimura, S., Jenkins, A., Regan, H., Holland, P. R., Assmann, K. M., Whitt, D. B., Van Wessem, M., van de Berg, W. J., Reijmer, C. H., and Dutrieux, P.: Oceanographic Controls on the Variability of Ice-Shelf Basal Melting and Circulation of Glacial Meltwater in the Amundsen Sea Embayment, Antarctica, *J. Geophys. Res. Oceans*, 122, 10131–10155, <https://doi.org/10.1002/2017JC012926>, 2017.
- Leclerc, A. J. and Labeyrie, L.: Temperature dependence of the oxygen isotopic fractionation between diatom silica and water, *Earth Planet. Sci. Lett.*, 84, 69–74, [https://doi.org/10.1016/0012-821X\(87\)90177-4](https://doi.org/10.1016/0012-821X(87)90177-4), 1987.
- 215 Lécuyer, C., Gardien, V., Rigaudier, T., Fourel, F., Martineau, F., and Cros, A.: Oxygen isotope fractionation and equilibration kinetics between CO₂ and H₂O as a function of salinity of aqueous solutions, *Chem. Geol.*, 264, 122–126, <https://doi.org/10.1016/j.chemgeo.2009.02.017>, 2009.
- van der Linden, E. C., Le Bars, D., Lambert, E., and Drijfhout, S.: Calibration of basal melt on past ice discharge lowers projections of Antarctica’s sea level contribution, *Ice sheets/Antarctic*, <https://doi.org/10.5194/tc-2021-348>, 2021.
- 220 van der Linden, E. C., Le Bars, D., Lambert, E., and Drijfhout, S.: Antarctic contribution to future sea level from ice shelf basal melt as constrained by ice discharge observations, *The Cryosphere*, 17, 79–103, <https://doi.org/10.5194/tc-17-79-2023>, 2023.
- Mallett, H. K. W., Boehme, L., Fedak, M., Heywood, K. J., Stevens, D. P., and Roquet, F.: Variation in the Distribution and Properties of Circumpolar Deep Water in the Eastern Amundsen Sea, on Seasonal Timescales, Using Seal-Borne Tags, *Geophys. Res. Lett.*, 45, 4982–4990, <https://doi.org/10.1029/2018GL077430>, 2018.
- 225 Mankoff, K. D., Jacobs, S. S., Tulaczyk, S. M., and Stammerjohn, S. E.: The role of Pine Island Glacier ice shelf basal channels in deep-water upwelling, polynyas and ocean circulation in Pine Island Bay, Antarctica, *Ann. Glaciol.*, 53, 123–128, <https://doi.org/10.3189/2012AoG60A062>, 2012.
- 230 Masson-Delmotte, V., Hou, S., Ekaykin, A., Jouzel, J., Aristarain, A., Bernardo, R. T., Bromwich, D., Cattani, O., Delmotte, M., Falourd, S., Frezzotti, M., Gallée, H., Genoni, L., Isaksson, E., Landais, A., Helsen, M. M., Hoffmann, G., Lopez, J., Morgan, V., Motoyama, H., Noone, D., Oerter, H., Petit, J. R., Royer, A., Uemura, R., Schmidt, G. A., Schlosser, E., Simões, J. C., Steig, E. J., Stenni, B., Stievenard, M., van den Broeke, M. R., van de Wal, R. S. W., van de Berg, W. J., Vimeux, F., and White, J. W. C.: A Review of Antarctic Surface Snow Isotopic Composition: Observations, Atmospheric Circulation, and Isotopic Modeling*, *J. Clim.*, 21, 3359–3387, <https://doi.org/10.1175/2007JCLI2139.1>, 2008.
- 235 Meredith, M. P., Brandon, M. A., Wallace, M. I., Clarke, A., Leng, M. J., Renfrew, I. A., van Lipzig, N. P. M., and King, J. C.: Variability in the freshwater balance of northern Marguerite Bay, Antarctic Peninsula: Results from $\delta^{18}\text{O}$, *Deep-Sea Res. II*, 55, 309–322, <https://doi.org/10.1016/j.dsr2.2007.11.005>, 2008.
- Meredith, M. P., Wallace, M. I., Stammerjohn, S. E., Renfrew, I. A., Clarke, A., Venables, H. J., Shoosmith, D. R., Souster, T., and Leng, M. J.: Changes in the freshwater composition of the upper ocean west of the Antarctic Peninsula during the first decade of the 21st century, *Prog. Oceanogr.*, 87, 127–143, <https://doi.org/10.1016/j.pcean.2010.09.019>, 2010.
- 240 Meredith, M. P., Falk, U., Bers, A. V., Mackensen, A., Schloss, I. R., Ruiz Barlett, E., Jerosch, K., Silva Busso, A., and Abele, D.: Anatomy of a glacial meltwater discharge event in an Antarctic cove, *Philos. Trans. R. Soc. Math. Phys. Eng. Sci.*, 376, 20170163, <https://doi.org/10.1098/rsta.2017.0163>, 2018.
- 245 Naveira Garabato, A. C. N., Forryan, A., Dutrieux, P., Brannigan, L., Biddle, L. C., Heywood, K. J., Jenkins, A., Firing, Y. L., and Kimura, S.: Vigorous lateral export of the meltwater outflow from beneath an Antarctic ice shelf, *Nature*, 542, 219–222, <https://doi.org/10.1038/nature20825>, 2017.

- Östlund, H. G. and Hut, G.: Arctic Ocean water mass balance from isotope data, *J. Geophys. Res. Oceans*, 89, 6373–6381, <https://doi.org/10.1029/JC089iC04p06373>, 1984.
- Paolo, F. S., Fricker, H. A., and Padman, L.: Volume loss from Antarctic ice shelves is accelerating, *Science*, 348, 327–331, <https://doi.org/10.1126/science.aaa0940>, 2015.
- 250 Paolo, F. S., Padman, L., Fricker, H. A., Adusumilli, S., Howard, S., and Siegfried, M. R.: Response of Pacific-sector Antarctic ice shelves to the El Niño/Southern Oscillation, *Nat. Geosci.*, 11, 121–126, <https://doi.org/10.1038/s41561-017-0033-0>, 2018.
- Paolo, F. S., Gardner, A., Greene, C., Nilsson, J., Schodlok, M., Schlegel, N., and Fricker, H.: Widespread slowdown in thinning rates of West Antarctic Ice Shelves, *Ice sheets/Antarctic*, <https://doi.org/10.5194/egusphere-2022-1128>, 2022.
- 255 Pritchard, H. D., Ligtenberg, S. R. M., Fricker, H. A., Vaughan, D. G., van den Broeke, M. R., and Padman, L.: Antarctic ice-sheet loss driven by basal melting of ice shelves, *Nature*, 484, 502–505, <https://doi.org/10.1038/nature10968>, 2012.
- Randall-Goodwin, E., Meredith, M. P., Jenkins, A., Yager, P. L., Sherrell, R. M., Abrahamsen, E. P., Guerrero, R., Yuan, X., Mortlock, R. A., Gavahan, K., Alderkamp, A.-C., Ducklow, H., Robertson, R., and Stammerjohn, S. E.: Freshwater distributions and water mass structure in the Amundsen Sea Polynya region, *Antarctica, Elem. Sci. Anthr.*, 3, 000065, <https://doi.org/10.12952/journal.elementa.000065>, 2015.
- 260 Rignot, E. and Jacobs, S. S.: Rapid Bottom Melting Widespread near Antarctic Ice Sheet Grounding Lines, *Science*, 296, 2020–2023, <https://doi.org/10.1126/science.1070942>, 2002.
- Rignot, E., Velicogna, I., Van Den Broeke, M. R., Monaghan, A., and Lenaerts, J.: Acceleration of the contribution of the Greenland and Antarctic ice sheets to sea level rise, *Geophys. Res. Lett.*, 38, 1–5, <https://doi.org/10.1029/2011GL046583>, 2011.
- 265 Rignot, E., Mouginot, J., Scheuchl, B., van den Broeke, M., van Wessem, M. J., and Morlighem, M.: Four decades of Antarctic Ice Sheet mass balance from 1979–2017, *Proc. Natl. Acad. Sci.*, 116, 1095–1103, <https://doi.org/10.1073/pnas.1812883116>, 2019.
- Rohling, E. J.: PALEOCEANOGRAPHY, PHYSICAL AND CHEMICAL PROXIES | Oxygen Isotope Composition of Seawater, in: *Encyclopedia of Quaternary Science*, Elsevier, 915–922, <https://doi.org/10.1016/B978-0-444-53643-3.00293-4>, 2013.
- 270 Rubin, S. I., Takahashi, T., Chipman, D. W., and Goddard, J. G.: Primary productivity and nutrient utilization ratios in the Pacific sector of the Southern Ocean based on seasonal changes in seawater chemistry, *Deep Sea Res. Part Oceanogr. Res. Pap.*, 45, 1211–1234, [https://doi.org/10.1016/S0967-0637\(98\)00021-1](https://doi.org/10.1016/S0967-0637(98)00021-1), 1998.
- 275 Schaffer, J., Timmermann, R., Arndt, J. E., Steinhage, D., and Kanzow, T.: RTopo-2: A global dataset of ice sheet topography, cavity geometry and ocean bathymetry to study ice-ocean interaction in Northeast Greenland, in: EPIC3REKLIM conference “Our Climate - Our Future”, Berlin, Germany, 2014-10-06-2014-10-09, REKLIM conference “Our Climate - Our Future,” Berlin, Germany, 2014.
- 280 Schneider, D. P., Steig, E. J., van Ommen, T. D., Dixon, D. A., Mayewski, P. A., Jones, J. M., and Bitz, C. M.: Antarctic temperatures over the past two centuries from ice cores, *Geophys. Res. Lett.*, 33, <https://doi.org/10.1029/2006GL027057>, 2006.

- Shepherd, A., Gilbert, L., Muir, A. S., Konrad, H., McMillan, M., Slater, T., Briggs, K. H., Sundal, A. V., Hogg, A. E., and Engdahl, M. E.: Trends in Antarctic Ice Sheet Elevation and Mass, *Geophys. Res. Lett.*, 46, 8174–8183, <https://doi.org/10.1029/2019GL082182>, 2019.
- 285 Silvano, A., Rintoul, S. R., Peña-Molino, B., Hobbs, W. R., Wijk, E. van, Aoki, S., Tamura, T., and Williams, G. D.: Freshening by glacial meltwater enhances melting of ice shelves and reduces formation of Antarctic Bottom Water, *Sci. Adv.*, 4, eaap9467, <https://doi.org/10.1126/sciadv.aap9467>, 2018.
- Skrzypek, G. and Ford, D.: Stable Isotope Analysis of Saline Water Samples on a Cavity Ring-down Spectroscopy Instrument, *Environ. Sci. Technol.*, 48, 2827–2834, <https://doi.org/10.1021/es4049412>, 2014.
- 290 Steig, E. J., Mayewski, P. A., Dixon, D. A., Kaspari, S. D., Frey, M. M., Schneider, D. P., Arcone, S. A., Hamilton, G. S., Blue Spikes, V., Mary Albert, Meese, D., Gow, A. J., Shuman, C. A., White, J. W. C., Sneed, S., Flaherty, J., and Wumkes, M.: High-resolution ice cores from US ITASE (West Antarctica): development and validation of chronologies and determination of precision and accuracy, *Ann. Glaciol.*, 41, 77–84, <https://doi.org/10.3189/172756405781813311>, 2005.
- Tamsitt, V., England, M. H., Rintoul, S. R., and Morrison, A. K.: Residence time and transformation of warm Circumpolar Deep Water on the Antarctic continental shelf, *Geophys. Res. Lett.*, e2021GL096092, <https://doi.org/10.1029/2021GL096092>, 2021.
- Thomas, E. R., Dennis, P. F., Bracegirdle, T. J., and Franzke, C.: Ice core evidence for significant 100-year regional warming on the Antarctic Peninsula, *Geophys. Res. Lett.*, 36, <https://doi.org/10.1029/2009GL040104>, 2009.
- 300 Thurnherr, A. M., Jacobs, S. S., Dutrieux, P., and Giulivi, C. F.: Export and circulation of ice cavity water in Pine Island Bay, West Antarctica, *J. Geophys. Res. Oceans*, 119, 1754–1764, <https://doi.org/10.1002/2013JC009307>, 2014.
- Velicogna, I., Sutterley, T. C., and Broeke, M. R. van den: Regional acceleration in ice mass loss from Greenland and Antarctica using GRACE time-variable gravity data, *Geophys. Res. Lett.*, 41, 8130–8137, <https://doi.org/10.1002/2014GL061052>, 2014.
- 305 Wählin, A. K., Graham, A. G. C., Hogan, K. A., Queste, B. Y., Boehme, L., Larter, R. D., Pettit, E. C., Wellner, J., and Heywood, K. J.: Pathways and modification of warm water flowing beneath Thwaites Ice Shelf, West Antarctica, *Sci. Adv.*, 7, eabd7254, <https://doi.org/10.1126/sciadv.abd7254>, 2021.
- Walker, S. A., Azetsu-Scott, K., Normandeau, C., Kelley, D. E., Friedrich, R., Newton, R., Schlosser, P., McKay, J. L., Abdi, W., Kerrigan, E., Craig, S. E., and Wallace, D. W. R.: Oxygen isotope measurements of seawater (H₂ 18O/H₂ 16O): A comparison of cavity ring-down spectroscopy (CRDS) and isotope ratio mass spectrometry (IRMS), *Limnol. Oceanogr. Methods*, 14, 31–38, <https://doi.org/10.1002/lom3.10067>, 2016.
- 310 WCRP Global Sea Level Budget Group: Global sea-level budget 1993–present, *Earth Syst. Sci. Data*, 10, 1551–1590, <https://doi.org/10.5194/essd-10-1551-2018>, 2018.
- Webber, B. G. M., Heywood, K. J., Stevens, D. P., Dutrieux, P., Abrahamsen, E. P., Jenkins, A., Jacobs, S. S., Ha, H. K., Lee, S. H., and Kim, T. W.: Mechanisms driving variability in the ocean forcing of Pine Island Glacier, *Nat. Commun.*, 8, 14507, <https://doi.org/10.1038/ncomms14507>, 2017.